October 2, 2017

CERN-SPSC-2017-033 / SPSC-EOI-017
02/10/2017

Measurement of associated charm production induced by 400 GeV/c protons

The SHiP Collaboration

Abstract

An important input for the interpretation of the measurements of the SHiP experiment is a good knowledge of the differential charm production cross section, including cascade production. This is a proposal to measure the associated charm production cross section, employing the SPS 400 GeV/c proton beam and a replica of the first two interaction lengths of the SHiP target. The detection of the production and decay of charmed hadron in the target will be performed through nuclear emulsion films, employed in an Emulsion Cloud Chamber target structure. In order to measure charge and momentum of decay daughters, we intend to build a magnetic spectrometer using silicon pixel, scintillating fibre and drift tube detectors. A muon tagger will be built using RPCs. An optimization run is scheduled in 2018, while the full measurement will be performed after the second LHC Long Shutdown.

The SHiP Collaboration

A. Akmete[46], A. Alexandrov[13], A. Anokhina[37], S. Aoki[17], E. Atkin[36], N. Azorskiy[27], J.J. Back[52], A. Bagulya[30], A. Baranov[38], G.J. Barker[52], M. Battistin[42(EN)], J. Bauche[42(TE)], A. Bay[44], V. Bayliss[49], G. Bencivenni[14], A.Y. Berdnikov[35], Y.A. Berdnikov[35], M. Bertani[14], C. Betancourt[45], I. Bezshyiko[45], O. Bezshyyko[53], D. Bick[8], S. Bieschke[8], A. Blanco[26], J. Boehm[49], M. Bogomilov[1], K. Bondarenko[53], W.M. Bonivento[12], J. Borburgh[42(TE)], A. Boyarsky[53], R. Brenner[41], D. Breton[4], R. Brundler[45], M. Bruschi[11], V. Büscher[9], A. Buonaura[45], L. Buonocore[d], S. Buontempo[14], S. Cadeddu[12], A. Calcaterra[14], M. Calviani[42(EN)], M. Campanelli[51], P. Chau[9], J. Chauveau[5], A. Chepurnov[37], M. Chernyavskiy[30], K.-Y. Choi[25], A. Chumakov[2], P. Ciambrone[14], K. Cornelis[42(BE)], M. Cristinziani[7], G.M. Dallavalle[11], A. Datwyler[45], N. D'Ambrosio[13,15], G. D'Appollonio[12,c], J. De Carvalho Saraiva[26], G. De Lellis[13,d], A. De Roeck[42], M. De Serio[10,a], L. Dedenko[37], P. Dergachev[32], A. Di Crescenzo[13,d], N. Di Marco[13], C. Dib[2], H. Dijkstra[42], V. Dmitrenko[36], S. Dmitrievskiy[27], D. Domenici[14], S. Donskov[33], A. Dubreuil[43], J. Ebert[8], M. Ehlert[6], T. Enik[27], A. Etenko[31], F. Fabbri[11], L. Fabbri[11,b], A. Fabich[42(EN)], O. Fedin[34], G. Fedorova[37], G. Felici[14], M. Ferro-Luzzi[42], R.A. Fini[10], P. Fonte[26], C. Franco[26], M. Fraser[42(TE)], R. Froeschl[42(HSE)], T. Fukuda[18], G. Galati[13,d], G. Gavrilov[34], S. Gerlach[6], B. Goddard[42(TE)], L. Golinka-Bezshyyko[53], A. Golovatiuk[53], D. Golubkov[28], A. Golutvin[50,44], D. Gorbunov[29], P. Gorbunov[28], S. Gorbunov[30], V. Gorkavenko[53], Y. Gornushkin[27], M. Gorshenkov[32], V. Grachev[36], E. Graverini[45], J.-L. Grenard[42(EN)], V. Grichine[30], N. Gruzinskii[34], A. M. Guler[46], Yu. Guz[33], C. Hagner[8], H. Hakobyan[2], E. van Herwijnen[42], A. Hollnagel[8], B. Hosseini[50], M. Hushchyn[38], G. Iaselli[10,a], A. Iuliano[13,d], R. Jacobsson[42], D. Joković[39], M. Jonker[42], I. Kadenko[53], C. Kamiscioglu[47], M. Kamiscioglu[46], M. Karaman[46], M. Khabibullin[29], G. Khaustov[33], A. Khotyantsev[29], S.H. Kim[21], V. Kim[34,35], Y.G. Kim[22], N. Kitagawa[18], J.-W. Ko[23], K. Kodama[16], A. Kolesnikov[27], D.I. Kolev[1], V. Kolosov[33], M. Komatsu[18], A. Kono[20], N. Konovalova[30], M.A. Korkmaz[46], I. Korol[6], I. Korol'ko[28], A. Korzenev[43], V. Kostyukhin[7], S. Kovalenko[2], I. Krasilnikova[32], K. Krivova[36], Y. Kudenko[29,36], P. Kurbatov[32], V. Kurochka[29], E. Kuznetsova[34], H.M. Lacker[6], A. Lai[12], G. Lanfranchi[14], O. Lantwin[50], A. Lauria[13,d], H. Lebbolo[5], K.S. Lee[24], K.Y. Lee[21], J.-M. Lévy[5], V. Likhacheva[29], L. Lopes[26], V. Lyubovitsky[2], J. Maalmi[4], A. Magnan[50], V. Maleev[34],

A. Malinin[31], Y. Manabe[18], M. Manfredi[42(GS)], A. Mefodev[29], P. Mermod[43], S. Mikado[19], Yu. Mikhaylov[33], D.A. Milstead[40], O. Mineev[29], A. Montanari[11], M.C. Montesi[13,d], K. Morishima[18], S. Movchan[27], N. Naganawa[18], M. Nakamura[18], T. Nakano[18], A. Nishio[18], A. Novikov[36], B. Obinyakov[31], S. Ogawa[20], N. Okateva[30], J. Osborne[42(GS)], M. Ovchynnikov[53], N. Owtscharenko[7], P.H. Owen[45], P. Pacholek[42(EN)], A. Paoloni[14], B.D. Park[21], S.K. Park[24], R. Paparella[10], A. Pastore[10,a], M. Patel[50], D. Pereyma[28], A. Perillo-Marcone[42(EN)], D. Petrenko[36], K. Petridis[48], D. Podgrudkov[37], V. Poliakov[33], N. Polukhina[30,36], M. Prokudin[28], A. Prota[13,d], A. Rademakers[42], A. Rakai[42(EN)], F. Ratnikov[38], T. Rawlings[49], M. Razeti[12], F. Redi[50], S. Ricciardi[49], M. Rinaldesi[42(EN)], Volodymyr Rodin[53], Viktor Rodin[53], T. Roganova[37], A. Rogozhnikov[38], H. Rokujo[18], G. Rosa[13], T. Rovelli[11,b], O. Ruchayskiy[3], T. Ruf[42], V. Samoylenko[33], A. Sanz Ull[42(TE)], A. Saputi[14], O. Sato[18], E.S. Savchenko[32], J. Schliwinski[6], W. Schmidt-Parzefall[8], N. Serra[45], S. Sgobba[42(EN)], O. Shadura[53], A. Shakin[32], M. Shaposhnikov[44], P. Shatalov[28], T. Shchedrina[30], L. Shchutska[53], V. Shevchenko[31], H. Shibuya[20], A. Shustov[36], S.B. Silverstein[40], S. Simone[10,a], R. Simoniello[9], M. Skorokhvatov[36,31], S. Smirnov[36], J.Y. Sohn[21], A. Sokolenko[53], E. Solodko[42(TE)], V. Solovev[35], N. Starkov[30], B. Storaci[45], P. Strolin[13,d], D. Sukhonos[42], Y. Suzuki[18], S. Takahashi[17], I. Timiryasov[44], V. Tioukov[13], D. Tommasini[42(TE)], M. Torii[18], N. Tosi[11], F. Tramontano[d], D. Treille[42], R. Tsenov[1,27], S. Ulin[36], A. Ustyuzhanin[38], Z. Uteshev[36], G. Vankova-Kirilova[1], F. Vannucci[5], P. Venkova[6], V. Venturi[42(EN)], S. Vilchinski[53], M. Villa[11,b], Heinz Vincke[42(DGS)], Helmuth Vincke[42(DGS)], K. Vlasik[36], A. Volkov[30], R. Voronkov[30], R. Wanke[9], J.-K. Woo[23], M. Wurm[9], S. Xella[3], D. Yilmaz[47], A.U. Yilmazer[47], C.S. Yoon[21], Yu. Zaytsev[28]

[1] *Faculty of Physics, Sofia University, Sofia, Bulgaria*
[2] *Universidad Técnica Federico Santa María and Centro Científico Tecnológico de Valparaíso, Valparaíso, Chile*
[3] *Niels Bohr Institute, University of Copenhagen, Copenhagen, Denmark*
[4] *LAL, Université Paris-Sud 11, CNRS/IN2P3, Orsay, France*
[5] *LPNHE, Université Pierre et Marie Curie, Université Paris Diderot, CNRS/IN2P3, Paris, France*
[6] *Humboldt-Universität zu Berlin, Berlin, Germany*
[7] *Universität Bonn, Bonn, Germany*
[8] *Universität Hamburg, Hamburg, Germany*
[9] *Johannes Gütenberg Universität Mainz, Mainz, Germany*
[10] *Sezione INFN di Bari, Bari, Italy*
[11] *Sezione INFN di Bologna, Bologna, Italy*
[12] *Sezione INFN di Cagliari, Cagliari, Italy*
[13] *Sezione INFN di Napoli, Napoli, Italy*
[14] *Laboratori Nazionali dell'INFN di Frascati, Frascati, Italy*
[15] *Laboratori Nazionali dell'INFN di Gran Sasso, L'Aquila, Italy*
[16] *Aichi University of Education, Kariya, Japan*
[17] *Kobe University, Kobe, Japan*
[18] *Nagoya University, Nagoya, Japan*

[19] *College of Industrial Technology, Nihon University, Narashino, Japan*
[20] *Toho University, Funabashi, Chiba, Japan*
[21] *Gyeongsang National University, Jinju, Korea*
[22] *Gwangju National University of Education* [e], *Gwangju, Korea*
[23] *Jeju National University* [e], *Jeju, Korea*
[24] *Korea University, Seoul, Korea*
[25] *Sungkyunkwan University* [e], *Gyeong GI-DO, Korea*
[26] *LIP, Universidade de Coimbra, Coimbra, Portugal*
[27] *Joint Institute of Nuclear Research (JINR), Dubna, Russia*
[28] *Institute of Theoretical and Experimental Physics (ITEP) NRC 'Kurchatov Institute', Moscow, Russia*
[29] *Institute for Nuclear Research of the Russian Academy of Sciences (INR RAS), Moscow, Russia*
[30] *P.N. Lebedev Physical Institute (LPI), Moscow, Russia*
[31] *National Research Centre 'Kurchatov Institute', Moscow, Russia*
[32] *National University of Science and Technology "MISiS", Moscow, Russia*
[33] *Institute for High Energy Physics (IHEP) NRC 'Kurchatov Institute', Protvino, Russia*
[34] *Petersburg Nuclear Physics Institute (PNPI) NRC 'Kurchatov Institute', Gatchina, Russia*
[35] *St. Petersburg Polytechnic University (SPbPU)* [f], *St. Petersburg, Russia*
[36] *National Research Nuclear University (MEPhI), Moscow, Russia*
[37] *Skobeltsyn Institute of Nuclear Physics of Moscow State University (SINP MSU), Moscow, Russia*
[38] *Yandex School of Data Analysis, Moscow, Russia*
[39] *Institute of Physics, University of Belgrade, Serbia*
[40] *Stockholm University, Stockholm, Sweden*
[41] *Uppsala University, Uppsala, Sweden*
[42] *European Organization for Nuclear Research (CERN), Geneva, Switzerland*
[43] *University of Geneva, Geneva, Switzerland*
[44] *École Polytechnique Fédérale de Lausanne (EPFL), Lausanne, Switzerland*
[45] *Physik-Institut, Universität Zürich, Zürich, Switzerland*
[46] *Middle East Technical University (METU), Ankara, Turkey*
[47] *Ankara University, Ankara, Turkey*
[48] *H.H. Wills Physics Laboratory, University of Bristol, Bristol, United Kingdom*
[49] *STFC Rutherford Appleton Laboratory, Didcot, United Kingdom*
[50] *Imperial College London, London, United Kingdom*
[51] *University College London, London, United Kingdom*
[52] *University of Warwick, Warwick, United Kingdom*
[53] *Taras Shevchenko National University of Kyiv, Kyiv, Ukraine*
[a] *Università di Bari, Bari, Italy*
[b] *Università di Bologna, Bologna, Italy*
[c] *Università di Cagliari, Cagliari, Italy*
[d] *Università di Napoli "Federico II", Napoli, Italy*
[e] *Associated to Gyeongsang National University, Jinju, Korea*
[f] *Associated to Petersburg Nuclear Physics Institute (PNPI), Gatchina, Russia*

Contents

1 Introduction

The accurate prediction of charm hadroproduction rates is an essential ingredient to establish the sensitivity of a high-intensity proton beam dump experiment like SHiP (Search for Hidden Particles) [1] to detect new particles possibly produced in charm decays and to make a precise estimate of the tau neutrino flux mostly produced in D_s decays.

The associated charm production can occur either directly from the interactions of the protons with the target or from subsequent interactions of the particles produced in the hadronic cascade. According to simulations [2], the contribution of secondary interactions increases the charm yield in the SHiP target by more than a factor two. However, no measurement of the cascade effect has been ever done. Moreover, there are currently no data concerning the angular and energy spectra of charmed hadrons produced from 400 GeV/c proton collisions.

In order to measure the different characteristics of charmed hadronic production in a SHiP-like target we propose a dedicated experiment to measure the double-differential cross section $d^2\sigma/(dEd\theta)$ and the hadronic cascade effect.

2 Theoretical motivations

It is well established that the hadroproduction of heavy quarks, i.e with mass much larger than the QCD scale (Λ_{QCD}), can be computed in the framework of perturbative QCD. Following the standard factorisation approach, the total cross section for heavy quark hadroproduction can be written as the convolution of three main ingredients:

- the parton distribution functions (pdf) of the colliding hadrons;
- the partonic hard scattering cross section;
- the fragmentation function, modeling the non-perturbative transition of a heavy quark to a specific hadron with heavy flavour.

Differential Next-to-Leading Order (NLO) calculations for the heavy quark hadroproduction at the partonic level are available in literature since long [3, 4, 5]. This machinery has proven to be successful in the qualitative and quantitative description of the top quark, the heaviest particle in the Standard Model (SM). The large value of its mass justifies the use of perturbation theory; moreover, unlike the case of charm and beauty, there is no need for a top quark fragmentation function since it decays semi-leptonically on a time scale much shorter than the typical hadronisation time.

The case of charm is more complicated. In Figure 1 a collection of its hadroproduction cross sections measured in fixed-target and collider experiments in a wide range of energies, is shown together with the NLO prediction. There is a general agreement

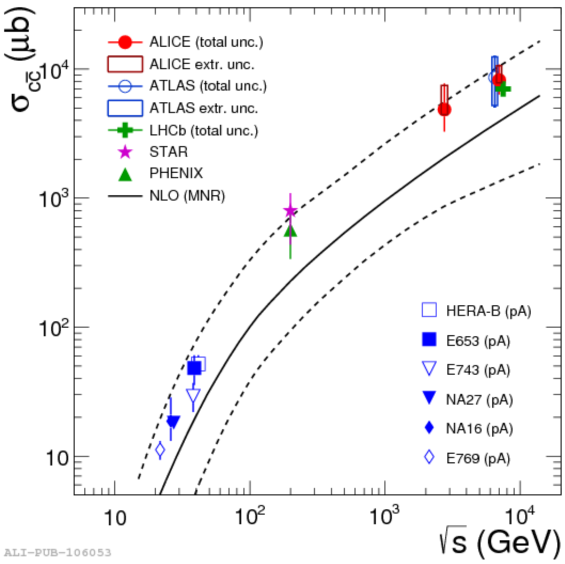

Figure 1: Collection of total inclusive charm production cross section measurements in nucleon-nucleon collisions as function of $\sqrt{s}$. NLO pQCD prediction (MNR[5]) and their uncertainties are shown as solid and dashed lines [6].

between data and theory within the estimated systematics. These systematics are typically dominated by large theoretical uncertainties: the renormalisation and factorisation scale dependence, the value of the heavy quark mass, and the uncertainties of the parton distribution functions.

Focusing on the configuration relevant for the SHiP experiment, i.e. a beam dump experiment with incoming protons at 400 GeV/c we report the experimental cross section as measured by NA27 [7] and the corresponding NLO predictions for typical choices of the charm mass and the renormalisation and factorisation scales in Table 1. The main source of uncertainty is given by the scale dependence, and in particular the dependence on the renormalisation scale, which gives a theoretical error from higher orders as large as an order of magnitude. The total cross section for charm hadroproduction is dominated

	exp NA27	th NLO ($m_c = 1.3$)	th NLO ($m_c = 1.5$)	th NLO ($m_c = 1.8$)
$\sigma[\mu\text{b}]$	18.1 ± 1.7	$24.3^{+80.1}_{-12.4}$	$10.1^{+22.6}_{-4.8}$	$3.12^{+4.86}_{-1.36}$

Table 1: Comparison between measurement and NLO predictions of the charm production total cross section in pp collisions with typical values of the charm mass (in GeV). The lower and upper values refer to renormalization (μ_R) and factorisation (μ_F) scale variations in the range $1/2 \leq \mu_R/\mu_F \leq 2$.

by the low p_T region, near the threshold given by the charm mass m_c. Since m_c is not so far above the $\Lambda_{\rm QCD}$ scale, the strong running coupling α_s is large and challenges the convergence of the perturbative expansion. Then, it is expected that higher order corrections give a large contribution, as confirmed by recent approximated calculations at the Next-to-Next-to leading order [8], and reflected in the large uncertainty given by the scale variations at NLO. Thus, perturbative QCD calculations have little predictive power for the total charm cross section in high-energy hadron-hadron collisions. In view of these theoretical issues, experimental measurements become necessary and in turn might be used to constrain the theoretical calculations. Indeed, as for the charm quark production, the SHiP experiment requires a well tuned Monte Carlo event generator to interpret the data. Monte Carlo Parton Shower (MCPS) programs have reached a high level of maturity and de-facto represent the standard event generators for collider physics. They go beyond fixed order calculations, resumming the leading collinear logarithm contributions to all orders in perturbation theory in the parton branching formalism. Moreover, they simulate the hadronisation process giving a full description of the hadronic final states. Although MCPS programs rely on leading order matrix elements for the description of the hard scattering process at the partonic level, they have a lot of parameters that can be adjusted to tune the simulation according to experimental data.

Different methods [9, 10, 11, 12, 13] have been developed to apply the NLO accuracy of the fixed-order calculations to the MCPS evolution. One might wonder why including more radiative content where pQCD has poor predictive power as mentioned above. As argued in [14, 15], despite the use of input parameters taken from data, the NLO calculation gives a better description of the p_T-spectrum and other differential distributions. To constrain the range of values for the unphysical renormalization and factorisation scales we adopt a procedure similar to the one followed in [16]. In this approach, the inclusive measurement of charm hadronic cross section at several energies are fitted with the NLO predictions. We select the collection of fixed target data reported in Table 2. The value of the charm quark mass is a tunable parameter, here fixed to $m_c = 1.27\,\mathrm{GeV}$ (PDG) to perform the prediction with relatively large factorisation scales, reducing the probability of backward evolution in the pdf evaluation. We use the NNPDF3.0_alphas_0118 pdf set and adopt a dynamical scale defined as $\mu_{\rm ref} = \sqrt{p_T^2 + m_c^2}$. The dynamical variable p_T is defined as the common transverse momentum of the heavy quark pair in the center-of-mass frame of the Born configuration, which represents the hardness of the short distance process. The result of our fit is shown in Figure 2 and it is summarized by the factorisation (μ_F) and renormalization (μ_R) bands: $0.66 < \frac{\mu_F}{\mu_{\rm ref}} < 3.24$, $1.38 < \frac{\mu_R}{\mu_{\rm ref}} < 1.74$, with the central value given by $\frac{\mu_F}{\mu_{\rm ref}} = 1.18$ and $\frac{\mu_R}{\mu_{\rm ref}} = 1.58$.

We use this scale variation band with the hvq event generator in the POWHEG framework [10] for NLO+PS computations (POWHEG+PYTHIA8.2).

At the characteristic energies of fixed target experiments the only available differential data have been provided by the E769 [17] experiment. As a consistency check in Figure 3 we compare these data with the uncertainty band as given by our fit, finding a rather good

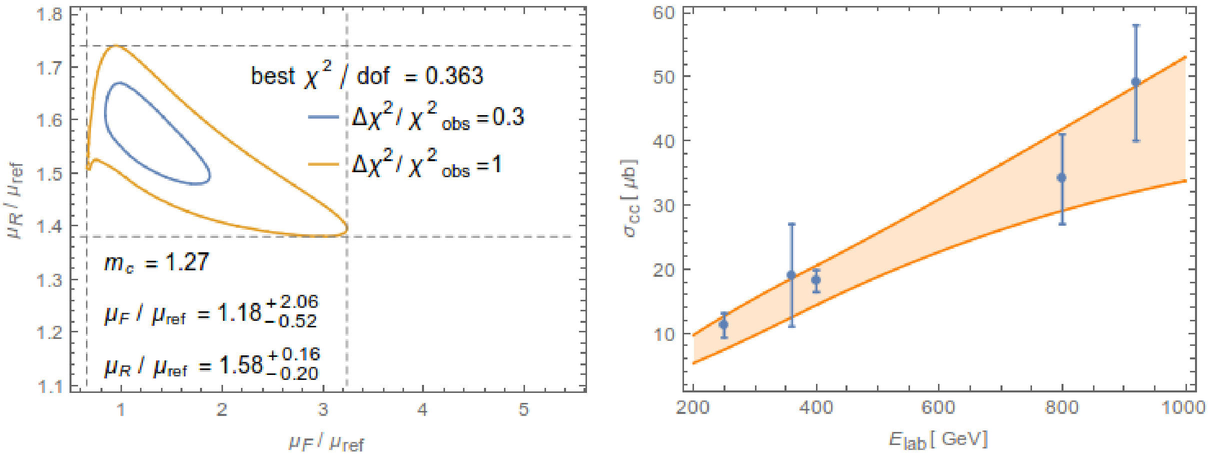

Figure 2: Left: contour plot for the reduced χ^2. The bands are defined by the rectangle including the contour $\Delta\tilde{\chi}^2 = 1$. Right: data points and the resulting uncertainty band.

agreement. In Figure 4 we show differential predictions for prompt charm production in proton-proton collisions at $Elab$ = 400 GeV, varying scales within the bands of our fit, the uncertainty on these distributions is of the order of 20%.

A 400 GeV/c proton beam dump produces charmed resonances from both prompt protons and secondary hadrons. Therefore we have to consider an iterative "cascade" of rescattering processes. A dedicated procedure has to be setup to describe this iterative process. For a rough estimate of this effect, we report an heuristic argument: given the probability P$\sim$40% that an energetic proton scatters through either an elastic (17%) or a diffractive (24%) process retaining a large fraction of its energy, the cascade effect can be estimated as 1/(1-P)$\sim$1.67. On top of this contribution, the charm yield from hadrons induced by inelastic proton collisions has to be added. An attempt to estimate the "cascade" effect based on experimental inputs and the PYTHIA MCPS program has been reported in [2]. That simulation leads to a charm yield a factor 2.3 times larger

Experiment	Elab(GeV)	σ [μb]
E769	250	$11.2 \pm 1.7 \pm 0.8$
NA16	360	$18.6\ +9.9\ -5.5$
NA27	400	18.1 ± 1.7
E743	800	$29 \pm 6 \pm 5$
E653	800	$48 \pm 6 \pm 11$
HERA-B	920	$51.7 \pm 5.8 \pm 6.6$

Table 2: Collection of measured total charm hadro-production cross sections.

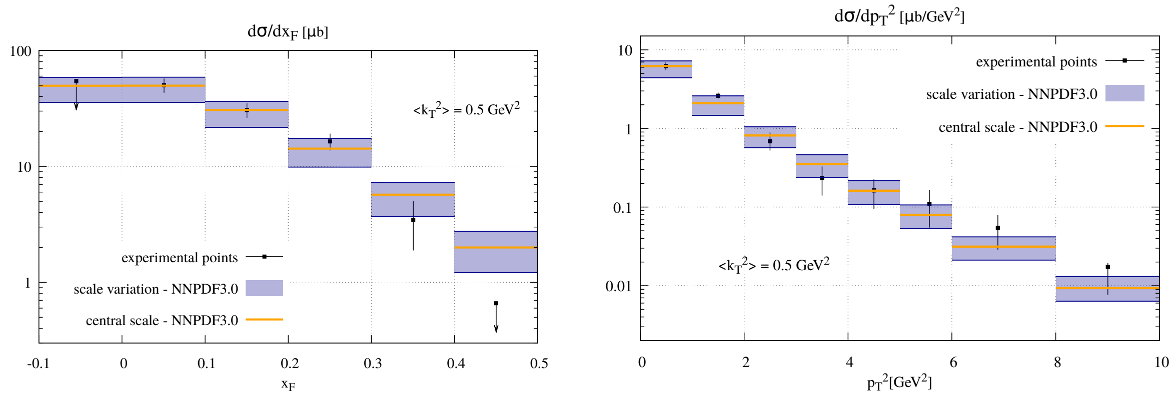

Figure 3: D meson (D^+, D^-, D^0, $\overline{D}^0$, D_s^+, D_s^-) single-inclusive distributions x_{F} (left) and p_T^2 (right) for production induced by p beam measured by E769 compared to the NLO QCD matched to parton shower predictions. Arrows indicate 90% confidence level upper limits.

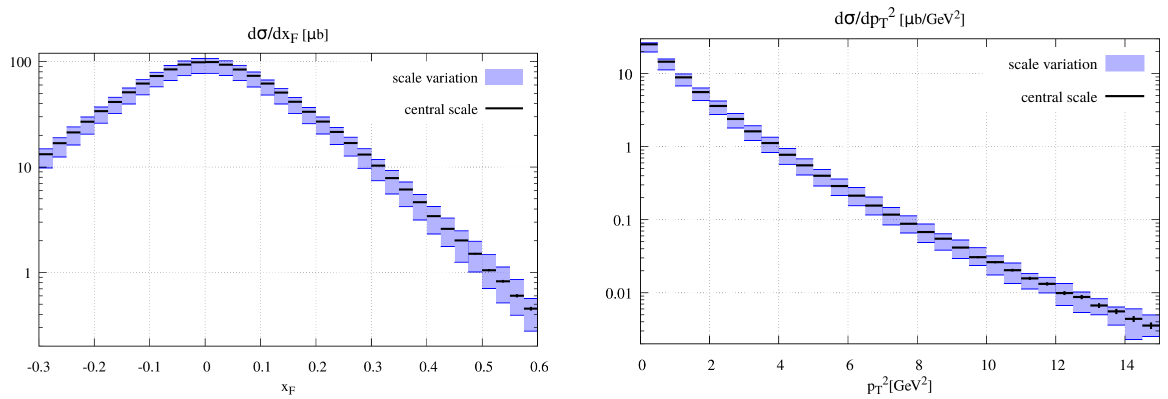

Figure 4: Predictions for D meson (D^+, D^-, D^0, $\overline{D}^0$, D_s^+, D_s^-) single-inclusive distributions x_{F} (left) and p_T^2 (right) for 400GeV proton collisions on target.

than the prompt contribution, with a softer energy spectrum for the secondary charmed hadrons. An accurate estimate of the uncertainty associated to the cascade effect requires a dedicated study. Nevertheless, assuming a comparable uncertainty of 20% in this factor, an overall uncertainty of about 30% is obtained when including the error in the prompt yield.

Finally, as mentioned above, a fully exclusive description in terms of hadronic final states is required for a full simulation of the expected signal yields in the SHiP detector. The transition from the partons to hadronic asymptotic states is controlled by non perturbative, long range, QCD dynamics. Within the factorisation approach, the non-perturbative content is modeled through scale-dependent universal fragmentation functions which parametrize the probability that a given quark fragments into a specific hadron species. In this context, universality means that the fragmentation functions do not depend upon the particular quark production mechanism. On the other hand, the factorisation theorem requires in general the presence of an high scale in the process or high transverse momentum transfer. Both conditions do not apply to the bulk of the associated charm production events in a beam dump experiment. Nevertheless there is so far no experimental evidence against factorisation. The most precise measurements of charm quark fragmentation fractions come from electron-positron annihilation (LEP [18]) and photo-production (ZEUSS [19] at HERA) processes. They are in good agreement providing a solid indication for universality.

For hadron-hadron processes at the relatively low energies of fixed-target experiments, the available level of statistics is not sufficient to perform an accurate analysis and to uncover any discrepancy. In Table 3, we report a collection of the available measurements. We remark that this list contains only experiments with pion beams. Those with protons are characterized by a lower statistics. Within the experimental uncertainties, they are consistent with the ones measured in electron-positron annihilation and photo-production. Nevertheless, several dynamical effects modeled with the introduction of phenomenological parameters in the MCPS programs, complicate the picture and make the interpretion more difficult: nuclear interactions, colour-drag effect, beam-remnants and other non-perturbative effects involved in the hadronisation process. On the other hand, the constraints given by the available measurements at LEP and HERA are weaker at the energies of interest, which are far below the Z pole. Indeed, the default Pythia set of parameters has been tuned according to LEP data, where the single string piece is characterized by a center-of-mass energy $\sim M_Z$. At the energy of interest for the SHiP case, the phase space is drastically reduced and thus the hadronisation model is used for an energy regime very different from the one used in the data fit. In this situation, several parameters can influence the final quark fragmentation fractions. Of course, by adjusting these parameters, it is possible to fine tune Pythia to reproduce new data at lower energies. Conversely, a new detailed measurement of charm fragmentation at low energies would be very important to establish the reliability of the factorisation assumption and of the hadronisation models.

3 Experimental layout

The SHiP experiment aims at searching for hidden particles and at observing a large statistics of tau neutrino events. The main source of both fluxes is the decay of charmed particles produced in the SHiP proton target [20]. The target will be composed of a mixture of TZM (titanium-zirconium doped molybdenum, 3.6 λ_I), tantalum (0.4 λ_I) and tungsten (7.7 λ_I).

We propose a new experiment to measure the charm cross section. Its conceptual design is shown in Figure 5. The 400 GeV/c SPS proton beam impinges on a replica of the SHiP target, instrumented using the Emulsion Cloud Chamber (ECC) technique: slabs of passive material are alternated with nuclear emulsion films. The emulsion films allow an accurate identification of the production and decay vertices of the charmed hadrons. Immediately downstream of the target a magnetic spectrometer is placed, designed to measure the momentum and the charge of the decay daughters, through their deflection in a magnetic field of around 1 T. The last component of the experiment is a muon filter, which is designed to identify muons with high efficiency. It will also measure the muon yield after the hadron absorber in a different layout configuration [21].
Detector performances were studied with simulations using FairShip, a framework designed for the SHiP experiment from FairRoot [22]. Associated charm production has been simulated taking into account not only direct production from proton interactions, but also secondary production from hadrons originated by the initial proton interaction [2].
The proposed location for this experiment is the North Area where several SPS extracted lines are available. In particular we have assumed to operate at H4, since the first data

Experiment	D^+/D^0	$D^0(\text{from } D^*)/D^0$	D_s^+/D^0
WA92: 350 GeV π^- on Cu	0.423 ± 0.012	0.280 ± 0.015	0.160 ± 0.037
WA92: 350 GeV π^- on W			0.183 ± 0.068
E769: 250 GeV π^- on Be, Al, Cu, W	0.419 ± 0.043	0.222 ± 0.031	
E769: 210 GeV π^- on Be, Al, Cu, W	0.258 ± 0.058		
E653: 600 GeV π^- on emulsion	0.393 ± 0.032		
NA32: 230 GeV π^- on Cu	0.422 ± 0.033	0.262 ± 0.026	
NA32: 200 GeV π^- on Si	$0.439^{\pm 0.123}_{-0.940}$	0.319 ± 0.095	
NA27: 360 GeV π^- on H	0.564 ± 0.171		

Table 3: Collection of measured production fraction of charmed resonances with respect the number of D^0 mesons.

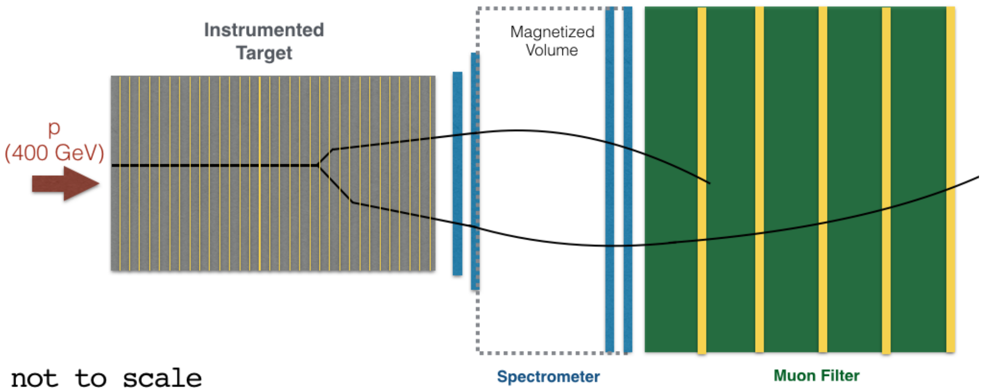

Figure 5: Sketch of the proposed experiment.

taking is planned in 2018 jointly with the muon flux measurement [21] and the two apparatuses share several sub-detectors. The Goliath magnet available in H4 will provide the magnetic field needed for the magnetic spectrometer.

The proposed layout of the SHiP-charm detector, as implemented in the FairShip simulation, is shown in Figure 6.

3.1 The target

3.1.1 SHiP target replica

The design of the SHiP target was optimised by the Beam Dump Facility (BDF) and target complex working groups of the Physics Beyond Colliders (PBS) study team [23]. It is cylindrical with a radius of 12.5 cm and a length of 150 cm. It is made of 13 slabs of TZM and 5 slabs of tungsten, along with 5-mm thick slits for water cooling. In order to prevent corrosion due to water cooling, each TZM and W slab will be tantalum cladded (1.5 mm on both sides). The target corresponds to a total of about 12 interaction lengths.

The proposed charm experiment aims at studying the associated charm production in a SHiP-like target with a rectangular transverse size (12.5×9.9 cm^2). The sequence of the passive material in blocks is retained as such but, since a much lower radiation dose is expected, water is replaced by PET slits since cooling is not needed.

Consequently, tantalum slabs are retained to preserve the number of interaction lengths as for the original SHiP target. For the measurement of associated charm production,

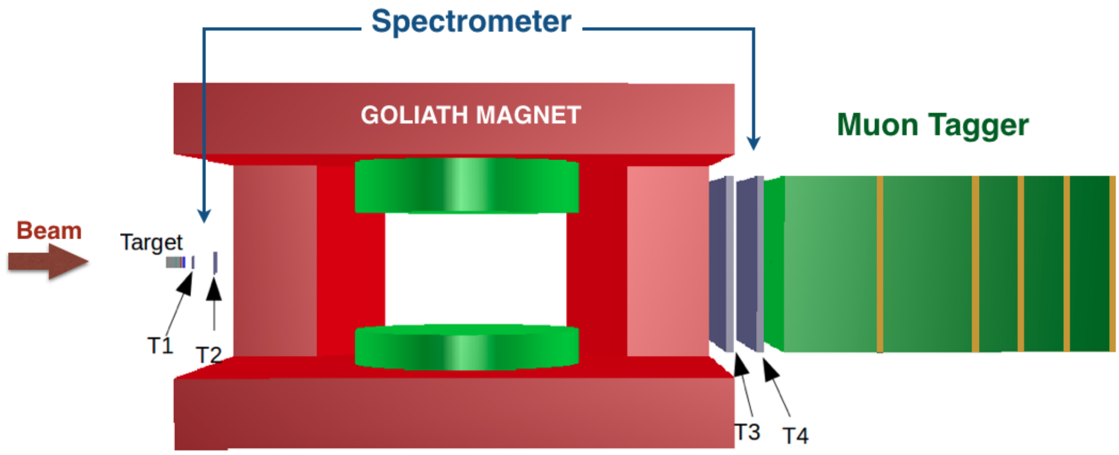

Figure 6: View of the experimental apparatus for the charm measurement.

such a replica of the SHiP target will be segmented in thinner slices interleaved with nuclear emulsion films that will act as a vertex and tracking detector with micrometric accuracy.

3.1.2 Segmentation of the target

In Figure 7 the position of charmed hadron production vertices along the beam direction in the target is shown, as obtained from simulation. The blue histogram represents the distribution of charmed hadrons produced in interactions of the primary protons, whereas the red histogram represents the distribution of charmed hadrons produced by the interaction of secondary hadrons produced in turn in the collision of primary protons. Since the number of charmed hadrons goes quickly to zero with the depth, measuring their production in the downstream part of the target would be very inefficient, in terms analysis time and signal-to-noise ratio. Focusing the analysis on the first 8 TZM slabs of the target, corresponding to $\sim$2 interaction lengths, allows to detect about 82% of the charm hadrons from primary production and 52% of those from cascade production, thus covering a significant fraction of both spectra.

The vertex detection is performed through the implementation of the Emulsion Cloud Chamber (ECC) technique: passive layers interleaved with nuclear emulsion films, allowing the detection of both production and decay of the charmed hadrons in the target. This technique has been successfully used in the OPERA [24] experiment and it will also be employed in the neutrino detector of the SHiP [1] experiment.

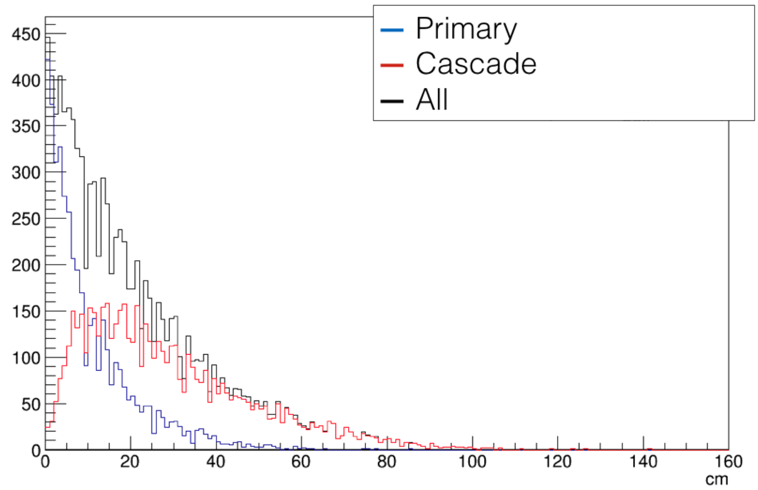

Figure 7: Distribution of the z coordinate of charmed hadrons production vertices along the SHiP target, from primary production (blue), cascade production (red) and the sum of the two components (black).

We intend to divide the target in five blocks, each corresponding to a fraction of interaction lengths between 0.25 and 0.28, as shown in Figure 8. The aforementioned segmentation of the SHiP target in TZM blocks is retained, but the first block of TZM, which is 78 mm thick, is divided in two smaller blocks. The number of PET and tantalum slits is retained.
During each run, some blocks of TZM, amounting to 0.2–0.3 interaction lengths of passive material, will be replaced by an ECC detector (Table 4), made of 1 mm slabs interleaved with thin emulsion films. The ECC detector is designed to cover almost the same interaction length of the passive blocks.
The ECC detector is the most downstream section of the target in each run, while the passive TZM blocks upstream are retained. So, in the first run the target is made only by ECC1, while in the other runs the ECC detector is placed after a certain amount of interaction lengths of passive material. Thus, the production of charmed particles as a function of the material thickness can be studied. The target composition in each run is shown in Table 5.

3.1.3 Track reconstruction in nuclear emulsions

The proposed emulsion films for this experiment consist of two 70μm-thick layers of nuclear emulsion, separated by a 175 μm-thick plastic base (Figure 9). The transverse size is 12.5×10 cm^2, like for the passive plates.
The track left by a charged particle on an emulsion layer is recorded by a series of sen-

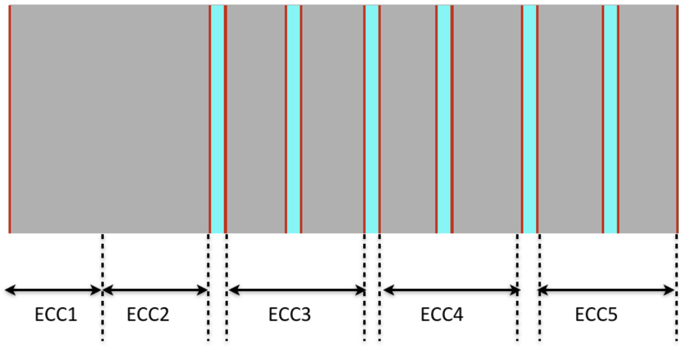

Figure 8: Layout of the SHiP target replica designed for the study of associated charm production.

Table 4: Composition of the five ECC detectors used in the experimental runs.

ECC	n TZM (1 mm)	λ	n PET (2.5 mm)	n Ta (1.5 mm)	n films
1	39	0.25	/	1	41
2	38	0.25	/	/	39
3	44	0.28	2	2	49
4	44	0.28	2	2	49
5	44	0.28	2	2	49

Table 5: Number of passive blocks and ECC for each configuration of the target.

Config	Passive					Active target
	n TZM (39 mm)	n TZM (38 mm)	n TZM (22 mm)	n PET (5 mm)	n Ta (1.5 mm)	
1	/	/	/	/	/	ECC1
2	1	/	/	/	1	ECC2
3	1	1	/	1	3	ECC3
4	1	1	2	3	7	ECC4
5	1	1	4	5	11	ECC5

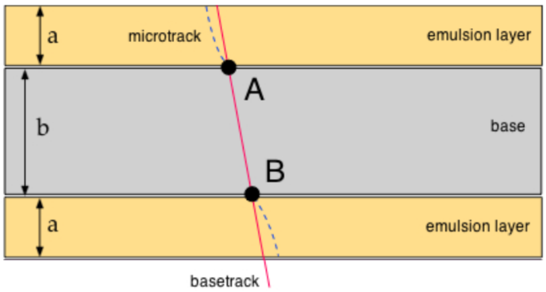

Figure 9: Layout of an emulsion film. Two 70 μm-thick layers of nuclear emulsions are separated by a 175 μm-thick plastic base.

sitisied AgBr crystals, growing up to 0.6 μm diameter during the development process. A new generation automated optical microscope [25] analyses the whole thickness of the emulsion, acquiring various topographic images at equally spaced depths. The acquired images are digitized, then an image processor recognizes the grains as *clusters*, i.e. groups of pixels of given size and shape. Thus, the track in the emulsion layer (usually referred to as *microtrack*) is obtained connecting clusters belonging to different levels. Since an emulsion film is formed by two emulsion layers, the connection of the two microtracks through the plastic base provides a reconstruction of the particle's trajectory in the emulsion film, called *base-track*. Most of the charged particles produced by the proton interactions are not related to the production and decay of charmed hadrons. These particles, leaving their traces in the emulsion film, may overlap with the grains left by the charmed hadrons and their daughters. Thus the density of deposited particles in the emulsion films has to be taken into account, when deciding the total number of protons on target in the experiment. Energy requirements and systems for particle tagging shall be studied too, in order to reject traces unrelated to the signal.
Different samplings are being considered, with the thickness of passive layers ranging from 1 to 3 mm. Longer thicknesses worsen the tracking performance but reduce the number of emulsion films to be analysed. The final sampling and thickness of ECC units will be decided after the 2018 optimization run [21].

3.1.4 Assembly procedure

We propose to assemble the emulsions and passive layers (TZM, Ta and PET slabs) using the packaging procedure adopted in the OPERA experiment and commonly referred to as 'spider packaging procedure'. It is based on a 800 μm thin aluminum foil, called 'spider', that provides mechanical stability to emulsion films and passive layers, which are stacked together to form a pile. The spider is firstly placed under the pile (Figure 10a), then it is folded on the sides by mechanical pressure (Figure 10b) and closed on the upper emulsion

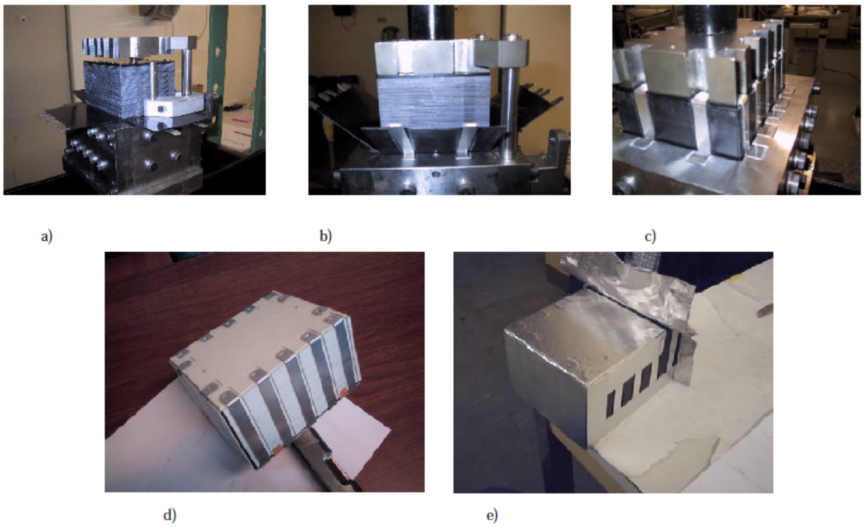

Figure 10: Sequence of the spider packaging procedure.

film (Figure 10c). Plastic side protection and cover keep the rigidity and avoid the direct contact between emulsions and aluminum (Figure 10d), the light shielding is provided by wrapping an adhesive aluminum tape around the pile (Figure 10e).

For the charm measurement, we plan to perform the preparation of the ECC target and subsequent development of the emulsion films in the emulsion laboratory at CERN, previously used by the OPERA experiment [26] (see Figure 11). The required spider and the press are already available (Figure 12), but they are designed to assemble targets of about the OPERA brick thickness (7.3 cm). We consider the possibility to adjust the configuration to match the OPERA brick size and also to use dedicated spiders.

3.2 Exposure

3.2.1 Target magnetization

The different portions of the target instrumented with nuclear emulsion films (ECC) constitute the downstream part of the target in order to maximise the number of charm decay products reaching the spectrometer. The target modules not instrumented with nuclear emulsions are retained upstream of the ECC. As an example, the schematic picture of ECC1 and ECC3 exposures is shown in Figure 13.

The electromagnetic showers produced in proton interactions in the target result in a large number of hits in the spectrometer stations, thus causing occupancy problems in the spectrometer planes. The particle multiplicity is dominated by soft electrons, that spoil the matching between nuclear emulsions and T1 station. In order to reduce the number of electrons we plan to keep the target within a magnetized region. A $\sim$10 cm gap between

Figure 11: The emulsion laboratory at CERN.

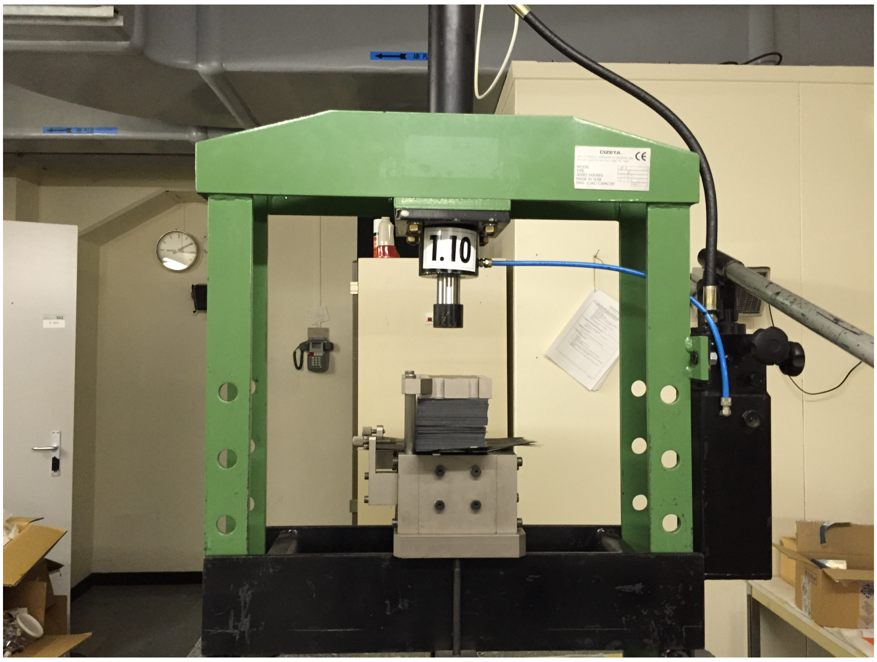

Figure 12: The press used in the emulsion laboratory at CERN to prepare the ECC target.

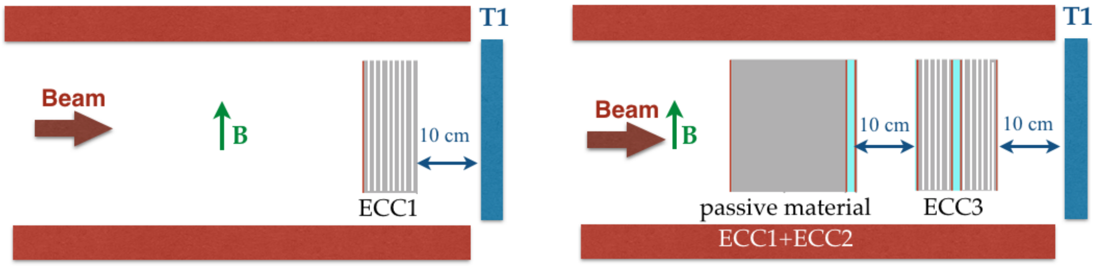

Figure 13: Schematic representation of the ECC1 (left) and ECC3 (right) exposures.

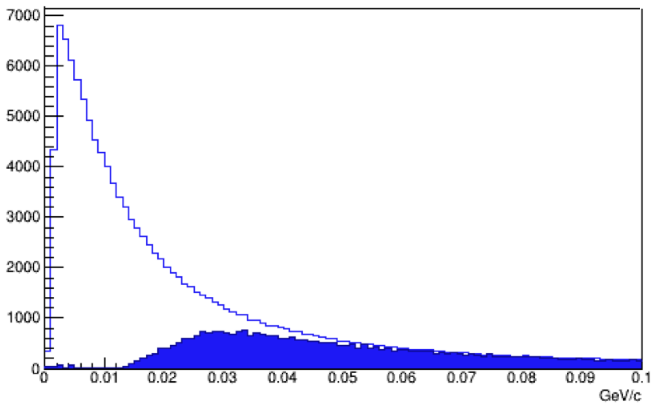

Figure 14: Momentum distributions of electrons in the T1 station, with (filled) and without (empty) magnetic field.

the ECC and the T1 station would deflect soft electrons thus reducing them by a factor $\sim$3 if a 1.5 T field is assumed. Figure 14 shows the momentum distributions of electrons in the T1 station, with and without magnetic field.

The number of charged tracks integrated in the emulsion films is the most important factor that limits number of integrated p.o.t. for each ECC. In the 2018 optimization run we plan to integrate a track density of 1×10^3 tracks/mm^2 and 3×10^3 tracks/mm^2 in order to test tracking and reconstruction algorithms in two different conditions.

The total number of charged particles (per p.o.t.) crossing the emulsion films located in the different ECCs is shown in Figure 15. Assuming a uniform distribution of the proton beam in the target surface, we can derive the expected track density and therefore evaluate the maximum of p.o.t. for each ECC (see Section 4.2).

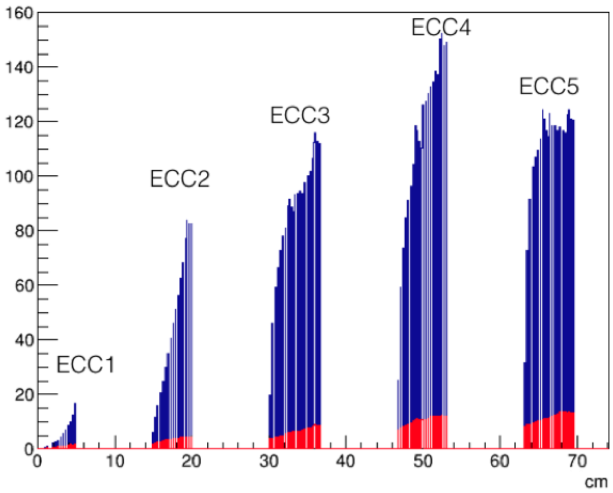

Figure 15: Number of integrated tracks in the emulsion films per proton on target, for the ECCs. The upper histogram includes all particles, whereas in the red histogram only the hadrons are considered.

3.2.2 Target mover

The proton beam is expected to have a Gaussian distribution ($\sigma = 0.5$ cm) in the two components of the transverse plane, with respect to the beam direction. This would lead to a much larger density of integrated tracks in the central region of nuclear emulsion films, thus strongly limiting the number of integrated protons on the target. In order to overcome this constraint and obtaining a uniform distribution of the proton interactions over the $\sim 12 \times 10$ cm^2 target surface, we plan to use a mechanical stage that moves the target in the transverse plane.

A first prototype of the target mover was tested at the very end of September 2017 at the H2 beam line using a 350 GeV/c proton beam with $\sigma \sim 0.4$ cm and an intensity of ∼4000 particles per spill. A picture of the target mover and the experimental setup is shown in Figure 16. The mechanical stage supporting an emulsion detector moves along the xy plane with a speed ranging from 0.001 to 50 mm/s. It was designed to withstand weights of ∼1 kg and to guarantee displacements up to 200 mm in both directions with an accuracy within 10μm.

The moving pattern is shown in Figure 17: during the spill, the target moves along x at the uniform speed of 3 cm/s, thus covering the whole target length along x in one spill. The movement along x axis is triggered by the *Start-of-Spill* signal form the SPS accelerator. Between two spills, the target moves along y axis. A 2 cm step along y axis was used in the test beam in order to study the beam profile. The total target surface was therefore covered in 6 spills. The stage spends 1 s to accelerate between 0 and 2 cm/s and another second to decelerate and to come back to its final position (Figure 18).

The mechanics of the target mover will be upgraded in order to support a $\sim$20 kg target, as required for the charm measurement.

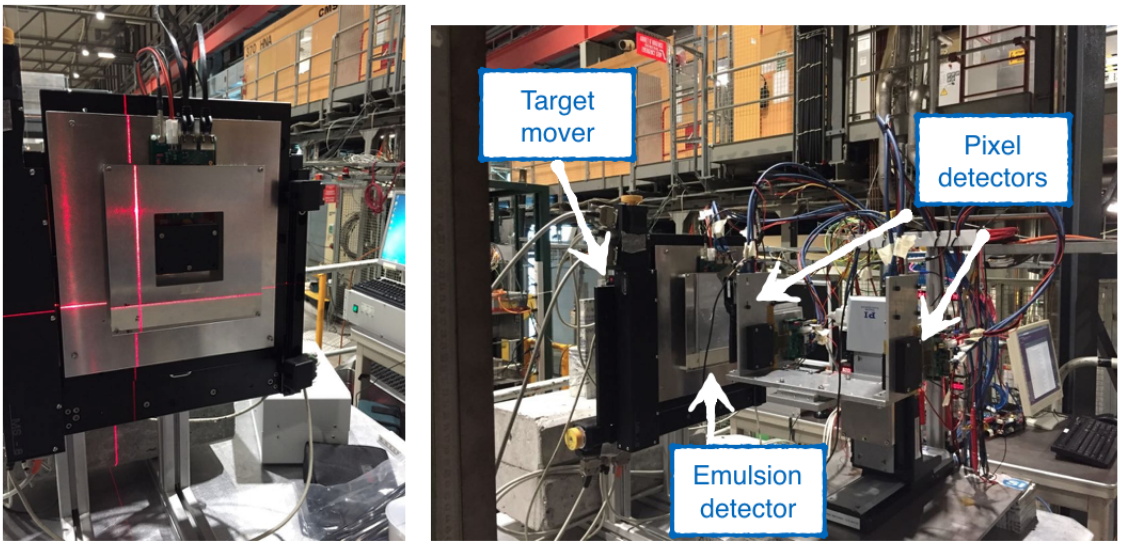

Figure 16: The moving table (left) and the September 2017 test beam experimental setup (right).

3.3 Magnetic Spectrometer

The proposed layout for the magnetic spectrometer is shown in Figure 6. It is made by four tracking stations, referred to as T1, T2, T3 and T4. We assume to use the Goliath magnet, permanently present in the H4 area, as the source of the magnetic field between T3 and T4 stations. Its dimensions are $3.6\times2.79\times4.5$ m^3 and the length of the magnetized region, along the beam axis, is $\sim$2 m between the two coils.

3.3.1 T1 and T2 stations

In order to cope with the high density of tracks between the target and the Goliath magnet the tracker stations T1 and T2 are required to be highly segmented and withstand a high occupancy. For these two stations we propose the use of hybrid silicon pixel detectors, of the same kind as currently successfully used in the Insertable B-Layer (IBL [27]) of the upgraded ATLAS detector.

The pixel modules consist each of a planar sensor and two custom developed large FE-I4 front-end chips [28] with a sophisticated readout architecture. The sensors are 200 μm thick n^+-in-n planar silicon pixel sensors with an inactive edge width of less than 450 μm,

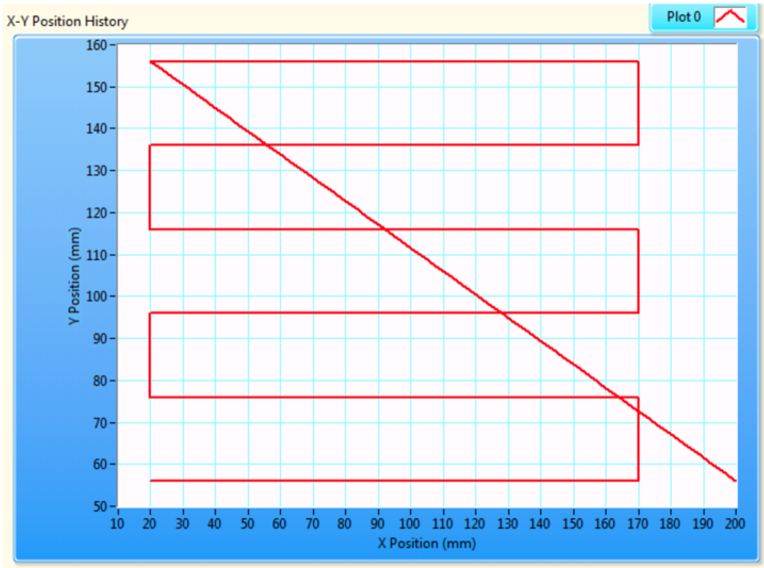

Figure 17: Measured pattern of the mechanical stage in the xy plane.

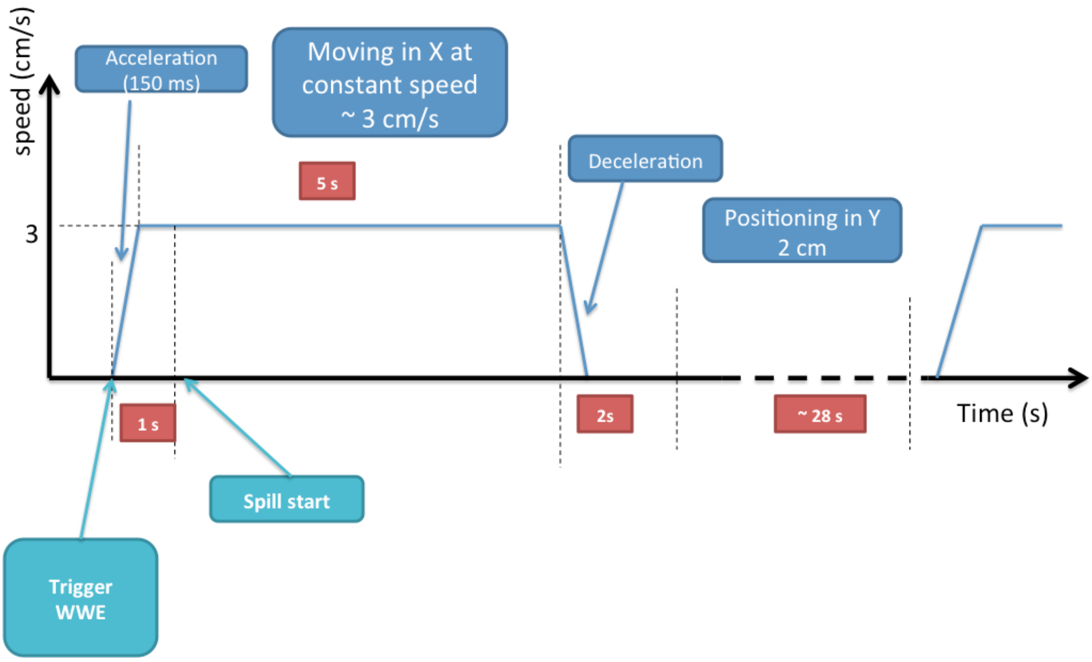

Figure 18: Temporal sequence of movements in a cycle.

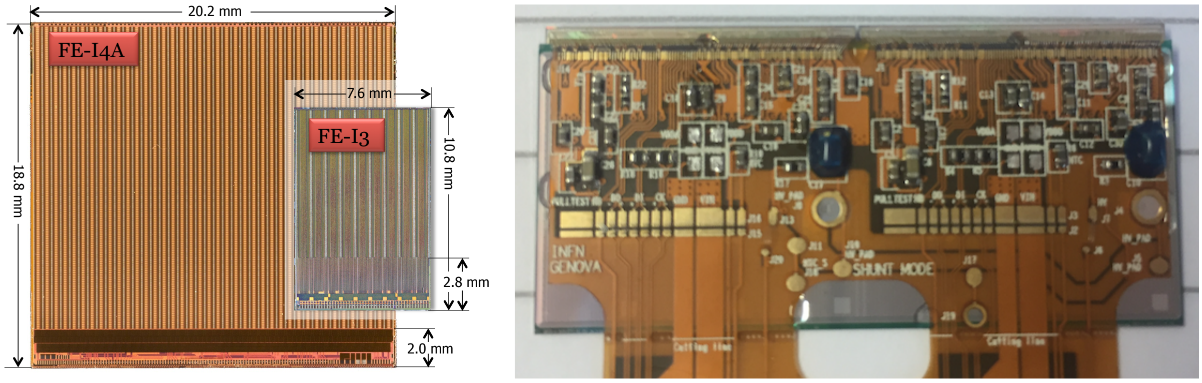

Figure 19: The large FE-I4 chip compared to its predecessor (left, [29]) and a photo of an assembled IBL pixel module (right), with two FE-I4 chips and a flex cable.

translating into a geometrical acceptance of 97.8%. The n^+ implantation is segmented into a matrix of 160 columns and 336 rows, of mostly 250 μm $\times$ 50 μm pixels. The outermost and central columns contain long pixels extended to 500 μm length. The front-end chip FE-I4 is built in a 130 nm CMOS feature size technology using thin gate oxide transistors to increase the radiation hardness. The large chip (20.2 mm $\times$ 18.8 mm) has an active area holding 80 columns with 336 pixels each and an approximately 2 mm high periphery, which results in an active over inactive area fraction of about 90%. The pixels have a size of 250 μm $\times$ 50 μm holding an analog and a digital circuitry. Modules consists of a sensor integrated to two FE-I4 IC via flip-chip bump-bonding, connecting each pixel on the sensor side to its dedicated FE-I4 pixel pre-amplifier input, via Ag-Sn solder bumps. The chip and a module are shown in Figure 19.

We plan to use 12–16 exisiting ATLAS IBL modules, 4–8 modules for the tracking station T1 and 8 modules for T2. For T1 the modules will be mounted pairwise, back-to-back onto an L-shaped aluminum support. The modules are oriented orthogonally to each other (see Figure 20). Depending on the number of available modules and space between the target and the Goliath magnet 2–4 such L-shaped supports will be installed for T1. The downstream T2 station will be equipped with two planes, each composed of four modules (two oriented along x-direction on the front side, two along y-direction on the rear side). Each track will thus be measured with up to 12 hits, half of them with high resolution (50 μm pitch), 4–8 hits in T1 and 4 hits in T2, depending on the configuration.

The readout system (USBPix) and the relative software, (pyBAR, Bonn ATLAS Readout in Python), are available, allowing to combine the readout of several planes and to record the data of all planes continuously. Finally, an online monitor provides an overview of the general status and performs online event building and hit correlation.

The connection between nuclear emulsions and the pixel modules was tested for the first time at the very end of September 2017 at the H2 beam line using a 350 GeV/c proton

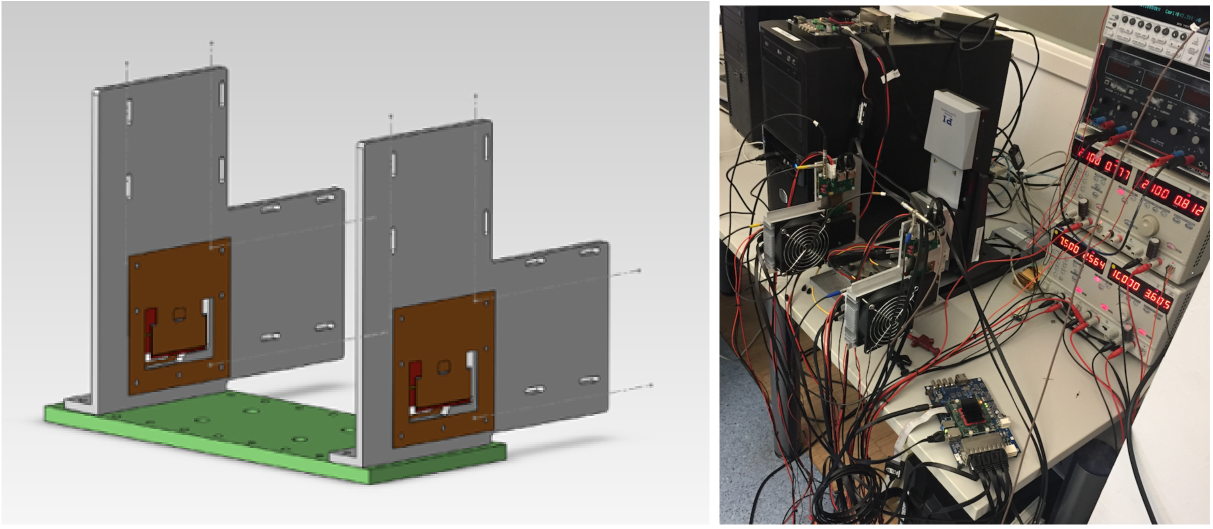

Figure 20: Drawing of the aluminum support structures (left) and picture of the four pixel modules, ready for the September 2017 test-beam (right).

beam. The experimental setup is shown in Figure 16. Data are going to be analysed.

3.3.2 T3 and T4 stations

For the T3 and T4 stations, we propose a combination of two different technologies: Scintillating Fibre trackers (SciFi) in the central 40×40 cm^2 region, where the density of tracks is higher, and drift tubes in the outer region, both being centered at z ∼480 and 510 cm from the target, respectively. Two modules per station are foreseen for the SciFi, each module consisting of two planes, in such a way to provide XU and YU coordinates: where U has a stereo angle of ∼2° with respect to X and Y, respectively.
Each detector plane is made of 3×12 cm wide *mats* of scintillating fibers. A *mat* is a matrix structure consisting of six staggered fibre layers with a horizontal pitch of 270 μm and a total length of 40 cm. The fibers are covered with a thin epoxy layer; titanium-dioxide is added to the epoxy to reduce channel-to-channel cross-talk. The layout of a SciFi module is shown in Fig. 21: *mats* in light green are mounted on a Carbon fibre and Rohacell structure, 12 silicon photomultipliers (SiPMs) are aligned to read out each plane being assembled on a flex cable PCB. They are meant to be connected through 40 cm flat cables to the readout chip housed outside the geometrical acceptance. The total material budget expected from a similar layout is ∼1-2%X0 for a double layer module.

The scintillating fibers are considered as the active detector elements, we intend to use Kuraray plastic double cladding scintillating fibers (SCSF-78MJ [30]) with a circular cross-section. The trapping efficiency in a single hemisphere is higher than 5.34% and the

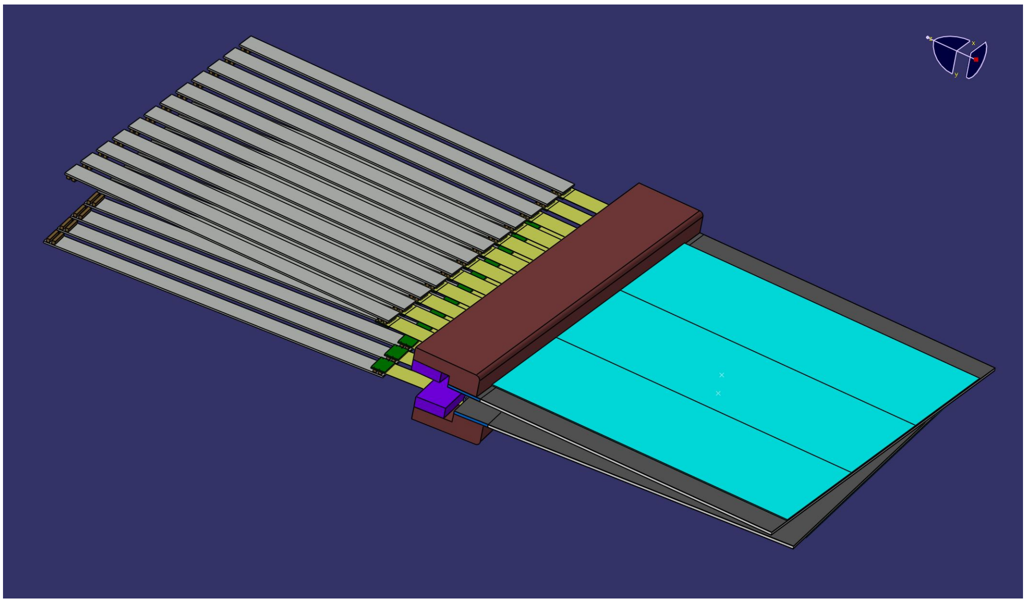

Figure 21: Layout of a SciFi module. In light blue three fibre *mats* per plane are assembled on a dark grey support structure. Two fastening pieces in brown and violet fix twelve SiPMs on each fibre plane, the SiPM detectors are assembled on flex pcbs in yellow. Flat cables in grey connect each flex pcb to the readout.

total diameter is 250 μm. The core of the fibre is polystyrene doped with p-terphenyl (PT) as primary dye, plus tetraphenyl-butadiene (TPB) as wavelength shifter. This choice was made to have a high quantum efficiency (>95%), decay time of the order of ns, and an emission wavelength spectrum from about 400 to 600 nm, peaking at 450 nm. The bulk optical absorption length is > 3.5 m.

The emission spectrum of the fibers is well suited for the Hamamatsu SiPM photo-detectors whose photo-detection efficiency peaks in the range 450 - 500 nm. The high optical absorption length and the good trapping efficiency allow observation of $\sim$20 photoelectrons per mm in the case of a scintillating fibre traversed by a charged particle on one side of the fibre, as seen on the opposite end. The SiPM detectors are composed of multichannel arrays; to minimise the over-all dead zones, two 64 channel silicon dies have been packaged into a SiPM array of 128 channels.

The channel width is 250 μm, slightly smaller than the fibre pitch, determining the granularity of the read-out. The 1.625 mm height of the channel covers the stack height for six layers of fibers. The active area is 200 μm higher than the total stack height of the fibers to cope with misalignment due to manufacturing tolerances. An epoxy protection layer, with a thickness of 100 -120 μm is placed between the end of the fibers and the silicon surface. The protection layer is advantageous for the handling of the detectors and to prevent ageing effects, such as corrosion, during long term operation. It limits

as well the signal cluster size. Indeed the signal is typically recorded by more than one detector channel; this phenomenon is due to the shift in the SiPM channels with respect to the fibre columns patterns, to air gap in between the fibre and the SiPM and optical cross talk among fibers. From simulation studies and previous experience from former detectors, the average cluster size is expected to be ~ 2.6 channels; this allows to cope with an occupancy of maximum 20 charged tracks per event in a single plane.
The characteristics of the signal and the noise are under study to evaluate the hit detection efficiency and spatial resolution. The latter is expected to be smaller than 100 μm, the former $\sim$99%. Inefficiency due to geometrical gaps and single dead channels is expected to be 1%, because the majority of the clusters have signals large enough for detection in more than one channel.
To reduce the effect of ghosts, a stereo angle is foreseen between the planes of $\sim 2°$; to further improve the hit ambiguities and reduce the low energy secondaries and noise background, time measurements are a valuable option under test.
Timing measurement with a time resolution of $\sim$1 ns can be achieved using the STiC readout chip [31], timing performance are limited by the dye decay time. The STiC is capable of handling 64 independent channels; for each channel self triggering, energy measurement by time over threshold and time to digital converter for timing info are provided. The digital output consists of time stamps to synchronise to other detectors. As DAQ system we would like to propose a new digital readout board, already in use for LHCb upgrade tests, developed by Tsinghua University and capable of a fast data transmission thanks to the output provided via Gigabit Ethernet.

Concerning the drift tubes in the external region, there are available prototypes from the muon spectrometer of the OPERA experiment [32]. The modules are currently being recommissioned and will be assembled into stations for the μ-flux measurement in 2018 [21]. The aluminium tubes have an outer diameter of 38 mm and a wall thickness of 0.85 mm. They are arranged in *modules* of 48 tubes, staggered in four layers of twelve tubes with a total width of approximatively 50 cm. A 45 µm gold-plated tungsten wire serves as an anode. The layout of the module is shown in figure 22.

The gas mixture adopted for the spectrometer was Argon and CO_2, in a mixing ratio of 80:20, which allowed to reach a maximum drift time of 1.3 µs. The spatial resolution achieved in the OPERA experiment was around 250 µm and, for tracks that pass through the tube near the anode wire, it was dominated by the drift velocity. Studies are currently ongoing about a faster and more linear drift gas mixture of $Ar{:}CO_2{:}N_2$, in a mixing ratio of $96 : 3 : 1$. Measurements of the spatial resolution achievable are ongoing.

3.4 Muon Tagger

The muon tagger is the most downstream detector in the apparatus. It has the task of identifying muons with high purity to tag the muonic decay channel of charmed hadrons.

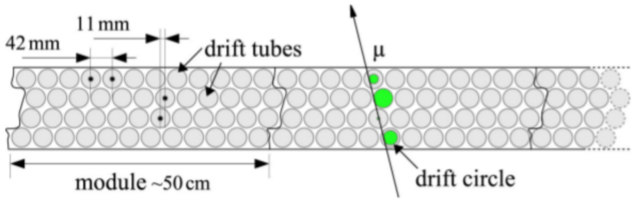

Figure 22: Sketch of the module layout [33]. A module consists of four layers with twelve tubes each. The end plates of a module are designed such that several modules can be combined.

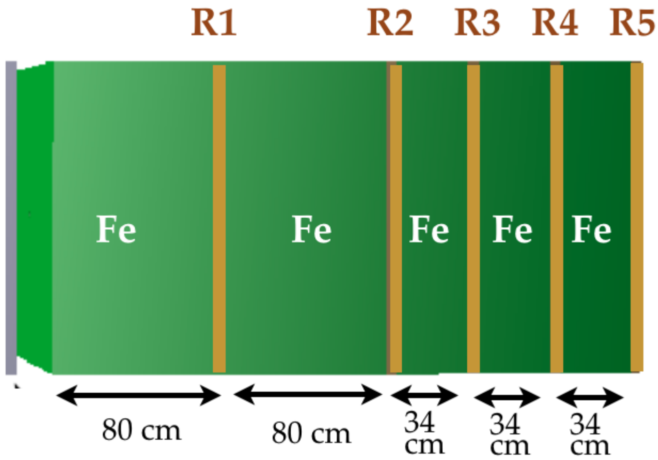

Figure 23: Layout of the muon tagger.

At the same time, it has to reconstruct the muon track slope to match the corresponding track reconstructed in the upstream Magnetic Spectrometer and assign the momentum to the muon track.

The layout of the muon tagger is shown in Figure 23. It is is made by five iron slabs: two 80 cm-thick and three 34 cm-thick, acting as hadron absorber, interleaved by five RPC planes, acting as trackers. The last three iron slabs could be replaced by ∼80 cm-thick concrete blocks. The transverse size of the RPC planes is 195×125 cm^2.

Since the target thickness covers at most two interaction lengths, we expect a large fraction of punch-through protons. In order to avoid their interactions in the iron slabs resulting in very high density regions in RPCs, a hole of 5 cm diameter will be drilled in the center of the iron slabs. In alternative, for concrete blocks, the hole could be made by the tapered corners of four (two by two) blocks in the center.

The RPCs for the muon tagger and the related electronics are being designed to serve as a module-0 for the SHiP experiment and will also be used for the μ-flux measurement

[21]. A small pilot production of new RPCs is foreseen. The gaps will have dimensions of 200 cm $\times$ 150 cm $\times$ 0.2 cm and the electrodes will be made of low-resistivity bakelite ($\simeq 10^{10}\Omega$ cm), 2 mm-thick, suited for operation in avalanche mode. The RPCs will be read out by means of orthogonal strip panels equipped with 1 cm-wide strips.

The signals from the strips will be collected by front-end electronics boards based on the FEERIC ASICS developed by the ALICE Collaboration [34], providing amplified and discriminated signals with LVDS output. The FEERIC ASICS is able to handle bipolar signals as those produced from readout strips arranged on both sides of each RPC. It is currently in production for the ALICE experiment.

The readout electronics uses boards equipped with LVDS input stage (64 channels) that can be operated in trigger-less mode providing zero-suppressed, 10 ns time-stamped signals that are transmitted via Ethernet interface (UDP/IP protocol) to the DAQ system. The boards are also able to provide a trigger signal generated as the logical OR (FAST OR) of the input LVDS signals. The trigger can be programmed based on groups of 32 channels.

The muon identification is done on the basis of the number of crossed layers in the detector. The distribution of the number of layers crossed by muons is reported in Figure 24a. If we normalize to the number of muons entering in the Muon Tagger, we get that about 77%, 72% and 69% of muons cross at least 3, 4 and five RPC layers, respectively.

In order to perform the tracking in the Muon Tagger, we require that the muon hits are *isolated* in at least two RPC planes. The isolation criterion requires at least 1 cm distance in both x and y coordinates with respect to the closest hit in the same RPC planes. About 67% of muons satisfy this requirement, as shown in Figure 24b, where the number of planes with isolated muon hits is reported.

3.5 Data acquisition system

The DAQ for the SHiP-charm experiment is designed to be simple and focused on maximising the data taking rate, at rates not exceeding 10 kHz. Its idea, illustrated in Figure 25, is to decouple system-specific readout from the central DAQ, whose role will be reduced to run control, event building and raw data storage. The sub-detectors (drift tubes, RPCs, pixel tracker, SciFi tracker) will be equipped with local DAQ machines or MCUs that will receive the central triggers, read out and buffer events during the spill, and between the spills send the event ‘blobs’, delimited by standard header and trailer, to the central DAQ. The target mover will receive the Start-of-Spill (SoS) and End-of-Spill (EoS) signals from the central trigger crate. It can also communicate with the central DAQ, sending the target position information that will be stored in the spill-related records.

The central DAQ will build full events, including the SoS and EoS events, and send them to a raw data recorder for saving on a sufficiently large local hard disk (optionally, RAID) storage. An unlimited number of asynchronous processes (on-line monitoring, event display, formatted event recorder) will have an access to the raw event buffer. The

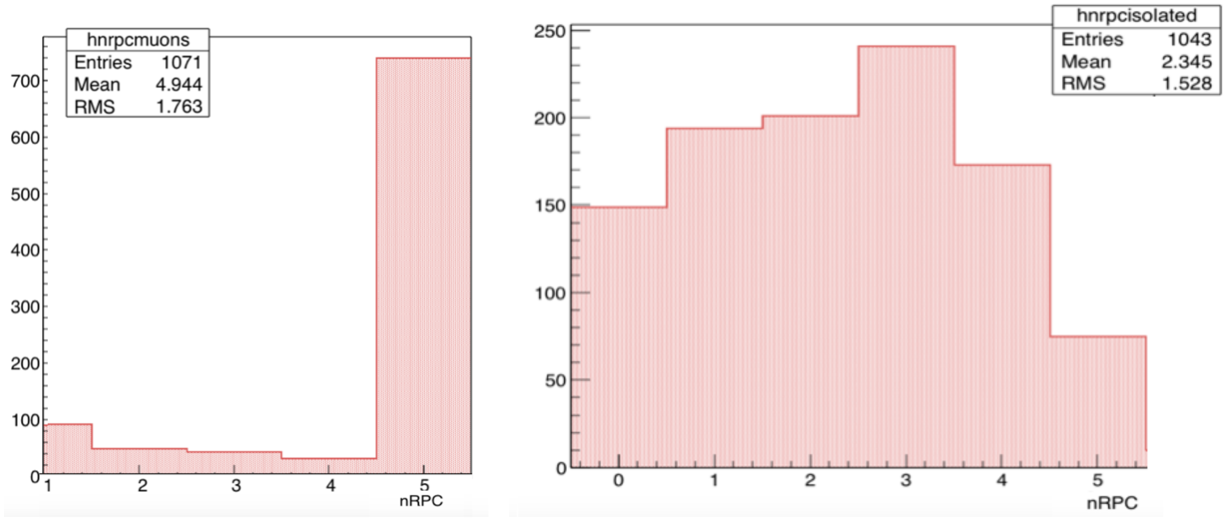

(a) (b)

Figure 24: (a) Number of RPC planes crossed by muons produced in charm decays. (b) Number of RPC planes where muon hits are isolated.

formatter process will transform the raw data stream into the format required for the offline processing and save the formatted data on the permanent mass storage.

A simple and light lossless communication mechanism (e.g., ContrlHost [35]) will be used for data and message exchange at all levels.

Within one run, the events will be identified by the spill number and trigger number within the spill. The central DAQ can communicate the spill number to all sub-systems at SoS. It is being defined whether individual triggers will be also tagged by the central DAQ, or rather counted by the sub-systems.

4 Signal and background evaluation

4.1 Charm detection in the target

The signal expectation was performed through simulation in the FairShip framework. The production of charmed hadrons was simulated with Pythia 6 [36] and the particle propagation in the materials with Geant4 [37] in the different target configurations.

Charmed hadrons have an average flight length of 3 mm, as shown in Figure 26. The charged track multiplicity at the charm decay vertex is shown in Figure 27a while the momentum distribution of charged decay daughters is reported in Figure 27b.

The first step for the signal identification is the location of the charmed hadron production vertex in the ECC. The vertex is considered located if it is made by at least two

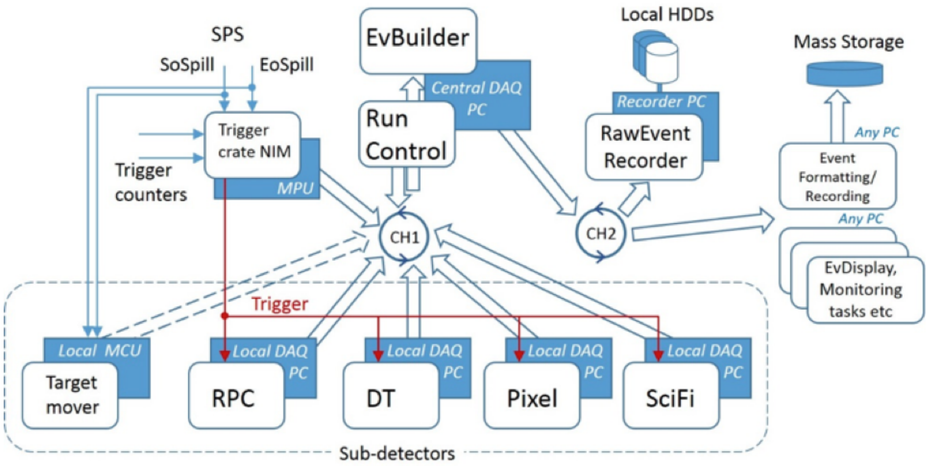

Figure 25: Schematic diagram of the proposed DAQ framework. CH1 and CH2 are the data buffers managed by the ControlHost, the former serving all synchronous and the latter asynchronous processes. CH1 and CH2 can run on different machines, but can be merged.

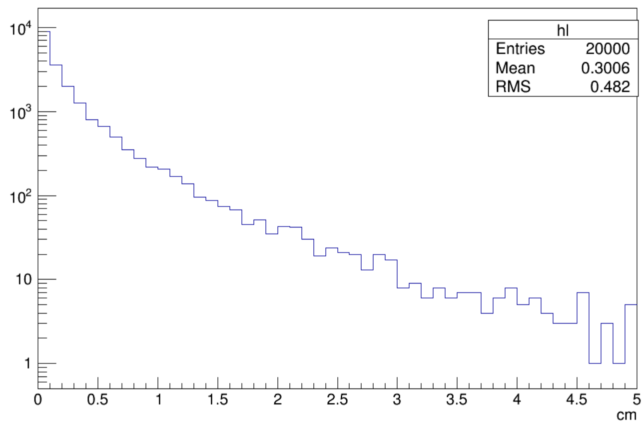

Figure 26: Flight length distribution of charmed hadrons.

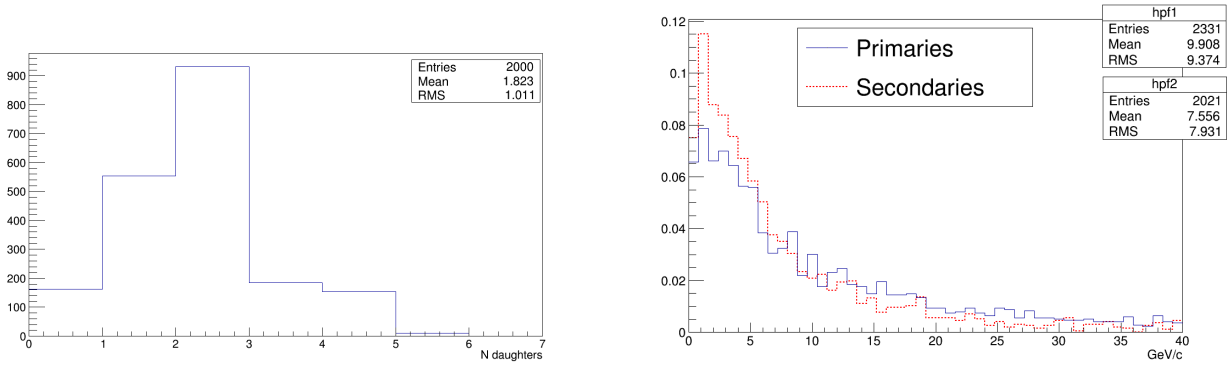

(a) (b)

Figure 27: (a) Number of charged decay daughters. (b) Momentum of charged decay daughters produced by the decay of a charmed hadron from primary proton interaction (blue) and from cascade production (dashed red).

charged tracks with a momentum larger than 100 MeV/c and an angle smaller than 1 rad. Among these tracks, at least one must have a momentum larger than 1 GeV/c .

The second step is the detection of the charmed hadron decay vertex. In order to take into account the geometrical acceptance of the ECC detector and the track reconstruction efficiency, we assume that only secondary vertices occurring at least three TZM slabs far from the downstream edge of the target are visible. The identification of a charmed hadron decay is performed through the so-called *decay search* procedure. It requires that the following criteria are satisfied:

- Impact parameter (IP) of decay daughter track with respect to the charmed hadron production vertex larger than 10 µm;
- kink angle larger than 20 mrad (only for 1-prong decays);
- at least one daughter track with momentum is larger than 100 MeV/c and angle smaller than 1 rad.

The identification of an associated charm production event requires the location of the charm production vertex and the detection of both charmed hadrons decay in the ECC. The associated charm detection efficiency in the ECC is of 29% and 35% for proton interactions occurring in the first and second interaction length, respectively.

The micrometric position resolution provided by nuclear emulsions allows to distinguish the different charm species (D^0, $D^{\pm}$, $D_s^{\pm}$, Λ_c^+). The D^0 is identified by the detection of a $V0$ topology, i.e. a secondary vertex with no visible parent. On the other hand, the measurement of the flight length allows to identify the different charged charmed hadrons

Table 6: Associated charm detection efficiency in ECC and number of associated charm events expected to be identified in the different ECCs, normalized to 10^5 p.o.t..

Configuration	Overall detection efficiency (%)	Expected events (per 10^5 p.o.t.)
ECC1	11	8
ECC2	11	6
ECC3	11	7
ECC4	12	5
ECC5	12	4

from their different mean free path ($c\tau_{D^\pm}$ = 311.8 μm, $c\tau_{D_s^\pm}$ = 149.9 μm, $c\tau_{\Lambda_c^+}$ = 59.9 μm).

4.2 Signal expectation

The predicted number of observed events has been estimated through the same FairShip simulation used to estimate the number of detected events in the ECC target. A detected event is considered observed if, for both charmed particles, at least one charged daughter is detected in all four planes of the magnetic spectrometer, thus allowing its charge and momentum measurements. The total efficiency, combining the information on the target and downstream detectors, and the predicted number of observed events per proton on target are shown in Table 6.

Due to the high multiplicity of particles per proton interaction (see Fig. 15) and the maximum track density affordable in the emulsions films, the number of proton interactions integrated in one ECC would not produce a sufficient statistics of charmed hadrons and therefore the exposure has to be repeated several times, by building and exposing many ECCs. Assuming a maximum track density in emulsions (10^3 particles/mm^2 or 3×10^3 particles/mm^2) we can derive the maximum number of p.o.t. integrated in each ECC and the corresponding number of observed charmed pairs, both reported in Table 7.

A possible exposure plan for the SHiP-charm experiment was derived for both track density conditions aiming at collecting 1000 fully reconstructed charmed hadron pairs with a balanced statistics at all target depths. The delivery of 2×10^7 p.o.t. would allow to reach this goal if 120 (40) runs are performed in the low (high) track density condition. The total emulsion surface required for the complete exposure amounts to 60 m^2 and 20 m^2 in the two cases, if a 1 mm sampling is assumed. Details are reported in Table 8.

We plan to collect about 10% of the total statistics in the 2018 optimization run.

Table 7: Maximum number of p.o.t. to be integrated in the different configurations (Npot) assuming a limit track density of 10^3 or 3×10^3 tracks/mm^2; Npair is the number of detected charm pairs expected for each configuration.

Config	Density=10^3 tr/mm^2		Density=3×10^3 tr/mm^2	
	Npot ($\times10^5$ pot)	Npair	Npot ($\times10^5$ pot)	Npair
1	7.5	58	22.5	175
2	1.5	10	4.5	29
3	1.0	7	3.0	22
4	0.8	5	2.4	14
5	1.0	4	3.0	13

Table 8: Number of runs (Nruns), total number of delivered pot (Npot) and number of expected charm pairs for each target configurations. Two limit track densities are considered.

Config	Density=10^3 tr/mm^2			Density=3×10^3 tr/mm^2		
	Nruns	Npot ($\times10^6$ pot)	Npair	Nruns	Npot ($\times10^6$ pot)	Npair
1	11	8.3	640	4	9.0	700
2	17	2.5	170	5	2.3	140
3	21	2.3	170	7	2.2	160
4	35	2.9	170	12	2.9	170
5	35	3.5	140	12	3.6	150
Total	119	19	1290	40	20	1320

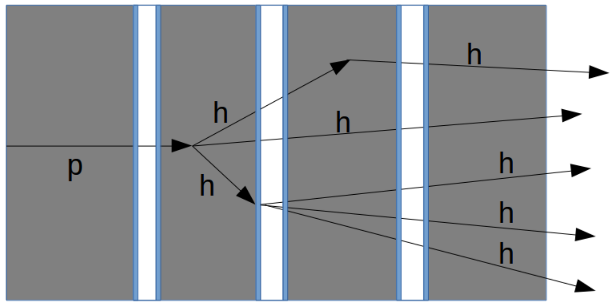

Figure 28: Sketch of a background event for the charm measurement.

4.3 Hadronic background

The event topology, as described in previous sections, is defined by a production vertex and two decay vertices, located in the ECC target. A hadron produced in the primary proton interaction could interact in the passive layers in the target, thus mimicking the decay vertex of a charmed particle. Hence, a proton interaction followed by two hadronic reinteractions constitutes a background source for the charm measurement (Figure 28). A Monte Carlo simulation in FLUKA [38] has been performed to study π^- interactions in a ECC target, where molybdenum slabs are interleaved with nuclear emulsion film. The transverse sizes of the target are 10×10 cm^2 and the passive sampling is 3 mm. The pion energy spectrum is provided, from the FairShip simulation, as an input for the FLUKA simulation. The relative distribution is shown in Figure 29. The distributions shown in Figure 30 represent the number of tracks and the number of nuclear fragments produced in the FLUKA simulation. The pion interactions which might mimick a decay of a charged charmed hadron are the 1-prong and 3-prong ones. Moreover, the observation of a nuclear fragment allows to recognize a hadronic interaction, thus providing good signal-background separation. The same topology selections chosen for the signal have been applied to the obtained background sampling, where the decay length of the charmed hadron is replaced by the track length of the pion, bounded to be smaller than 6 mm. Moreover, the events with one nuclear fragment are excluded, as well as events with an even number of prongs. Thus, the probability that a pion interaction is associated to the decay of a charmed hadron has been evaluated.

The background for the associated charm production detection comes from the reinteraction of two hadrons in the target, both mimicking the decay of a charmed particle. Thus, given the estimated probability and accounting for the hadron multiplicity, the fraction of proton interactions where at least two hadrons mimic a charmed hadron decay has been estimated to be 1.4×10^{-3}.

A refined statistical analysis based on machine learning techniques exploiting the signal and background characteristics will be used for signal to background discrimination. The pdfs of set of variables that can be used for this purpose are shown in Figure 31 for signal

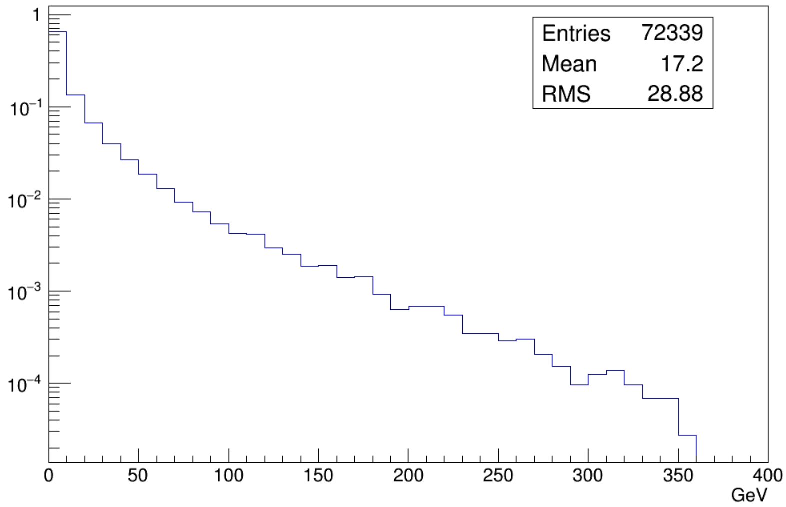

Figure 29: Kinetic energy distribution of charged pions, produced in 400 GeV/c proton interactions.

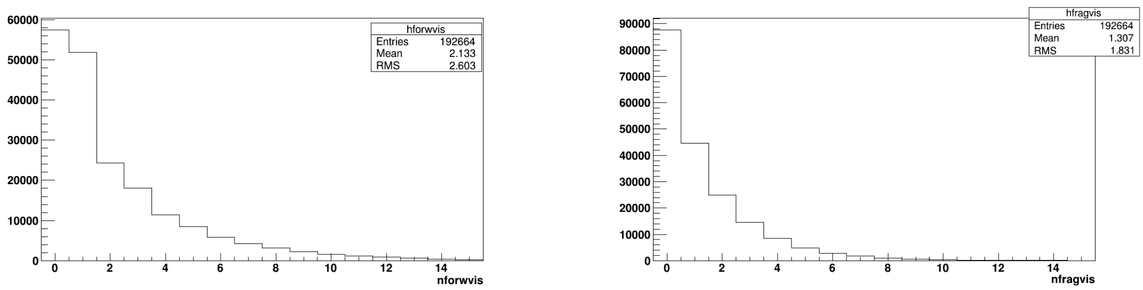

Figure 30: Number of tracks and nuclear fragments produced in each pion interaction in the ECC.

and background: track length, kink angle, impact parameter for 1-prong decays.

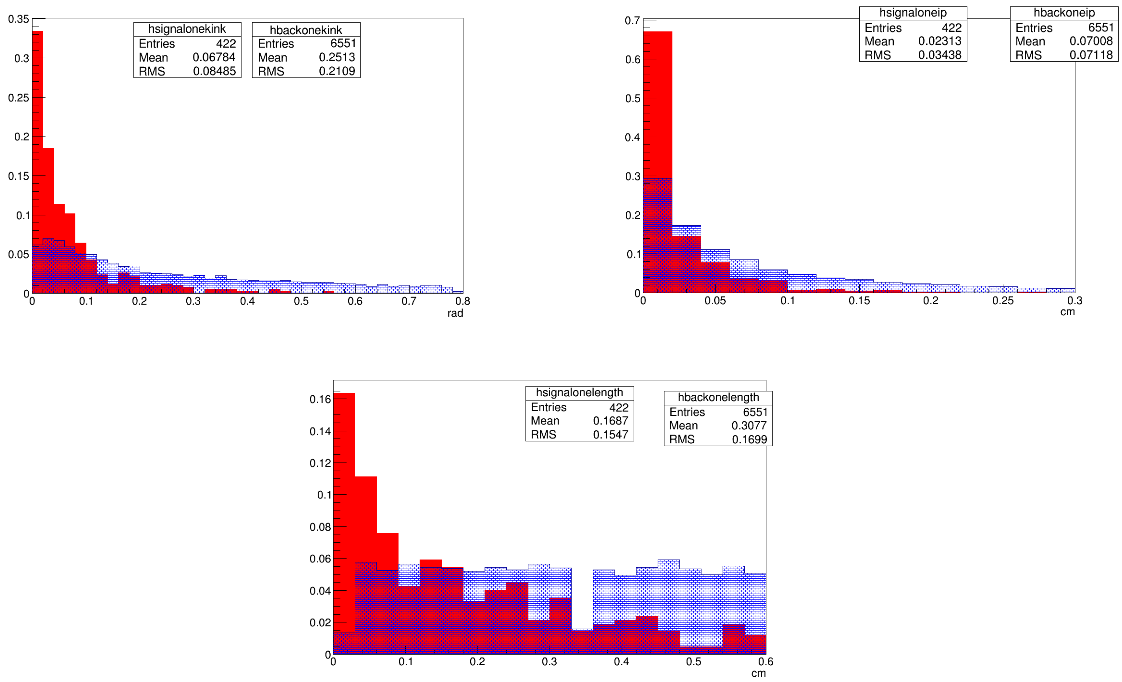

Figure 31: Distributions for signal (in red) and background (in blue) events: kink angle (top left), impact parameter (top right) and track length (bottom).

5 Beam requirements

About one week is needed to integrate the different sub-detectors. For the final measurement after LS2 we require about 5×10^7 400 GeV/c p.o.t. integrated during four weeks of data taking at the SPS. One week is required for the optimization run in 2018 with 5×10^6 p.o.t. to collect about 200 charmed hadron pairs.

The spill intensity has to be adjusted around $\sim10^4$ protons per spill and a beam with transverse size of σ $\sim$0.5 cm demonstrated to be feasible in the test performed at the end of September 2017.

6 Project management

Several SHiP groups have agreed to collaborate with the design and building of the apparatus required for the experiment described in this document:

- University and INFN of Bari: read-out electronics and mechanics of the RPC chambers of the muon tagger (S. Simone)
- University of Bonn: silicon pixel detector for the instrumentation of the T1 and T2 planes of the spectrometer (M. Cristinziani)
- University of Hamburg: spectrometer, drift tube commissioning and readout (D. Brick and S. Bieschke)
- KODEL Korea University: Gaps and strips production for the RPC chambers of the muon tagger (S. Park)
- EPFL Lausanne: Scintillator fiber option for the instrumentation of the T3 and T4 planes of the spectrometer (A. Bay)
- Lebedev Physical Institute, Moscow: production of emulsion films, data taking and emulsion analysis (N. Polukhina)
- National University of Science and Technology "MISIS", Moscow: SHiP target replica material (Y. Krasilnikova)
- University of Nagoya: Emulsion film production and analysis (M. Komatsu)
- University and INFN of Naples: emulsion analysis, front-end electronics for the RPC chambers of the muon tagger, target mover and overall coordination (G. De Lellis)
- University of Zurich: data taking and emulsion analysis (N. Serra)

In addition, CERN will take care of the design target replica (M. Calviani), integration and beam line (N. Charitonidis), radio protection (R. Froeschl).

An optimization run is scheduled in 2018 as expressed in the EoI-016 while the full run will be carried out after LS2.

7 Summary

The interpretation of the SHiP data requires a detailed knowledge of the differential charm production rates. Theoretical predictions for the total rate of prompt charm at the relevant energies are affected by large uncertainties of both perturbative and non-perturbative nature. A measurement could shed light on the impact of these contributions. In particular, the precise knowledge of the charm fragmentation fractions at such realativity low energy is missing and it is important to benchmark modern hadronization models. Furthermore, the measurement of charmed resonances produced in the interaction of secondary hadrons is missing and it is important to estimate the acceptance of any detector operating at a SPS beam dump facility. In this EoI we have reported the design of an apparatus with different sub-detectors to address this measurement with sufficient accuracy.

References

[1] M. Anelli et al. A facility to Search for Hidden Particles (SHiP) at the CERN SPS. *CERN-SPSC-2015-016, SPSC-P-350*, 2015.

[2] H Dijkstra and T. Ruf. Heavy Flavour Cascade Production in a Beam Dump. *CERN-SHiP-NOTE-2015-009*, 2015.

[3] P. Nason, S. Dawson, and R. Keith Ellis. The Total Cross-Section for the Production of Heavy Quarks in Hadronic Collisions. *Nucl. Phys.*, B303:607–633, 1988.

[4] P. Nason, S. Dawson, and R. Keith Ellis. The One Particle Inclusive Differential Cross-Section for Heavy Quark Production in Hadronic Collisions. *Nucl. Phys.*, B327:49–92, 1989. [Erratum: Nucl. Phys.B335,260(1990)].

[5] Michelangelo L. Mangano, Paolo Nason, and Giovanni Ridolfi. Heavy quark correlations in hadron collisions at next-to-leading order. *Nucl. Phys.*, B373:295–345, 1992.

[6] Jaroslav Adam et al. D-meson production in p-Pb collisions at $\sqrt{s_{\rm NN}}$ =5.02 TeV and in pp collisions at $\sqrt{s}$ =7 TeV. *Phys. Rev.*, C94(5):054908, 2016.

[7] M. Aguilar-Benitez et al. Charm Hadron Properties in 400-GeV/c p p Interactions. *Z. Phys.*, C40:321, 1988.

[8] M. V. Garzelli, S. Moch, and G. Sigl. Lepton fluxes from atmospheric charm revisited. *Journal of High Energy Physics*, 2015(10):115, Oct 2015.

[9] Stefano Frixione and Bryan R. Webber. Matching NLO QCD computations and parton shower simulations. *JHEP*, 06:029, 2002.

[10] Stefano Frixione, Paolo Nason, and Bryan R. Webber. Matching NLO QCD and parton showers in heavy flavor production. *JHEP*, 08:007, 2003.

[11] Paolo Nason. A New method for combining NLO QCD with shower Monte Carlo algorithms. *JHEP*, 11:040, 2004.

[12] Stefano Frixione, Paolo Nason, and Carlo Oleari. Matching NLO QCD computations with Parton Shower simulations: the POWHEG method. *JHEP*, 11:070, 2007.

[13] Simone Alioli, Paolo Nason, Carlo Oleari, and Emanuele Re. A general framework for implementing NLO calculations in shower Monte Carlo programs: the POWHEG BOX. *JHEP*, 06:043, 2010.

[14] Oleksandr Zenaiev et al. Impact of heavy-flavour production cross sections measured by the LHCb experiment on parton distribution functions at low x. *Eur. Phys. J.*, C75(8):396, 2015.

[15] Matteo Cacciari, Michelangelo L. Mangano, and Paolo Nason. Gluon PDF constraints from the ratio of forward heavy-quark production at the LHC at $\sqrt{S} = 7$ and 13 TeV. *Eur. Phys. J.*, C75(12):610, 2015.

[16] R. E. Nelson, R. Vogt, and A. D. Frawley. Narrowing the uncertainty on the total charm cross section and its effect on the J/ψ cross section. *Phys. Rev.*, C87(1):014908, 2013.

[17] G. A. Alves et al. Feynman x and transverse momentum dependence of D meson production in 250-GeV pi, K and p - nucleon interactions. *Phys. Rev. Lett.*, 77:2392–2395, 1996.

[18] Leonid Gladilin. Fragmentation fractions of c and b quarks into charmed hadrons at LEP. *Eur. Phys. J.*, C75(1):19, 2015.

[19] H. Abramowicz et al. Measurement of charm fragmentation fractions in photoproduction at HERA. *JHEP*, 09:058, 2013.

[20] Sergey Alekhin et al. A facility to Search for Hidden Particles at the CERN SPS: the SHiP physics case. *Rept. Prog. Phys.*, 79(12):124201, 2016.

[21] A. Akmete et al. μ-flux measurements for SHiP at H4. *CERN-SPSC-2017-020, SPSC-EOI-016*, 2017.

[22] M. Al-Turany, D. Bertini, R. Karabowicz, D. Kresan, P. Malzacher, T. Stockmanns, and F. Uhlig. The FairRoot framework. *J. Phys. Conf. Ser.*, 396:022001, 2012.

[23] BDF Group. Prototype target specifications. *https://edms.cern.ch/document/1823120/1*.

[24] R. Acquafredda et al. The OPERA experiment in the CERN to Gran Sasso neutrino beam. *JINST*, 4:P04018, 2009.

[25] A. Alexandrov et al. The Continuous Motion Technique for a New Generation of Scanning Systems. *Scientific Reports*, 7:7310, 2017.

[26] C. Sirignano. R&D on OPERA ECC: studies on emulsion handling and event reconstruction techniques. *Ph.D Thesis*, 2005.

[27] F. Hugging. The ATLAS Pixel Insertable B-Layer (IBL). *Nucl. Instrum. Meth.*, A650:45–49, 2011.

[28] M. Garcia-Sciveres et al. The FE-I4 pixel readout integrated circuit. *Nucl. Instrum. Meth.*, A636:S155–S159, 2011.

[29] ATLAS IBL Collaboration. Prototype ATLAS IBL Modules using the FE-I4A Front-End Readout Chip. *JINST*, 7:P11010, 2012.

[30] T.D. Beattie, A.P. Fischer, S.T. Krueger, G.J. Lolos, Z. Papandreou, E.L. Plummer, A.Yu. Semenov, I.A. Semenova, L.M. Sichello, L.A. Teigrob, and E.S. Smith. Light yield of kuraray scsf-78mj scintillating fibers for the gluex barrel calorimeter. *Nuclear Instruments and Methods in Physics Research Section A: Accelerators, Spectrometers, Detectors and Associated Equipment*, 767:245 – 251, 2014.

[31] T Harion, K Briggl, H Chen, P Fischer, A Gil, V Kiworra, M Ritzert, H C Schultz-Coulon, W Shen, and V Stankova. Stic a mixed mode silicon photomultiplier readout asic for time-of-flight applications. *Journal of Instrumentation*, 9(02):C02003, 2014.

[32] R. Zimmermann, J. Ebert, C. Hagner, B. Koppitz, V. Savelev, W. Schmidt-Parzefall, J. Sewing, and Y. Zaitsev. The precision tracker of the OPERA detector. *Nucl. Instrum. Meth.*, A555:435–450, 2005. [Erratum: Nucl. Instrum. Meth.A557,690(2006)].

[33] B. Buttner et al. Alignment methods for the OPERA drift tube detector. *Nucl. Instrum. Meth.*, A747:56–61, 2014.

[34] P. Dupieux, B. Joly, F. Jouve, S. Manen, and R. Vandaele. Upgrade of the ALICE muon trigger electronics. *JINST*, 9:C09013, 2014.

[35] R. Gurin and A. Maslennikov. ControlHost, Distributed Data Handling Package. *https://www.nikhef.nl/pub/experiments/antares/software/Dispatcher/Marseille-Oct95.ps.*

[36] Torbjorn Sjostrand, Stephen Mrenna, and Peter Z. Skands. PYTHIA 6.4 Physics and Manual. *JHEP*, 05:026, 2006.

[37] S. Agostinelli et al. GEANT4: A Simulation toolkit. *Nucl. Instrum. Meth.*, A506:250–303, 2003.

[38] Alfredo Ferrari, Paola R. Sala, Alberto Fasso, and Johannes Ranft. FLUKA: A multi-particle transport code (Program version 2005). *CERN-2005-010, SLAC-R-773, INFN-TC-05-11*, 2005.